Available online at www.sciencedirect.com
SCIENCE DIRECT®
Advances in Water Resources 27 (2004) 99–120
Advances in Water Resources
www.elsevier.com/locate/advwatres

Control volume function approximation methods and their applications to modeling porous media flow II: the black oil model ☆

Baoyan Li, Zhangxin Chen, Guanren Huan *

Department of Mathematics, Southern Methodist University, Box 750156, Dallas, TX 75275-0156, USA

Received 16 October 2003; received in revised form 9 December 2003; accepted 22 December 2003

Abstract

This is the second paper of a series where we introduce control volume function approximation (CVFA) methods and present their applications to modeling porous media flow. In the first paper, we introduced these methods to solve linear partial differential equations (PDE) in two-dimensional space and applied them to modeling two-phase flow. In this paper we extend them to solving coupled nonlinear PDEs in three-dimensional space and present their applications to reservoir simulation using the black oil model. The numerical results show that the CVFA methods are efficient and accurate for solving 'crossing bubble point' and three-phase coning problems. For a large model problem with over 20,000 nodes, the computational cost of the CVFA methods is virtually the same as that of the control volume finite element methods, slightly more than that of the 5-point finite difference (FD) method (the 7-point in three dimensions), and less than that of the 9-point FD method (the 11-point in three dimensions).

AMS: 35K60; 35K65; 76S05; 76T05
Keywords: Control volume function approximation; Black oil model; Porous media; Control volume finite element; Numerical experiments

1. Introduction

The control volume function approximation (CVFA) methods [6] are similar to the control volume finite element (CVFE) methods [3] in that the geometric elements they use are based on control volumes. The major difference between them is that the interpolation in the CVFA uses non-polynomial functions (e.g., spline, 'bilinear', and weighted distance functions), instead of polynomials utilized in the CVFE. The most advantageous feature of the CVFA methods is that the flux in a porous media flow problem is continuous across an interface between two neighboring control volumes. In general, however, this property is not preserved by the CVFE methods. Other features of the CVFA methods include: (1) they apply to arbitrarily shaped control volumes, (2) they reduce grid orientation effects, and (3) they conserve mass locally on each control volume.

In the first paper of this series [6], we introduced the CVFA methods to solve linear PDEs in two-dimensional space and applied them to modeling two-phase flow in porous media. In this paper, we extend them to solving coupled nonlinear PDEs in three-dimensional space, apply them to discretize the governing equations of the black oil model, and present numerical results for the benchmark problems of the first and second SPE comparative solution projects [8,12]. The black oil model consists of three phases, and includes compressibility and mass transfer effects [9].

The rest of this paper is constructed as follows. In the next section, we develop the CVFA methods in three-dimensional space. A brief discretization of the black oil model is given in the third direction. Numerical experiments are presented in the fourth section. Concluding remarks are given in the fifth section. Finally, the linearization of the governing equations and well control equations by the Newton–Raphson method and the discretization of these equations by the CVFA methods

☆ This work is supported in part by National Science Foundation grants DMS-9972147 and INT-9901498.
* Corresponding author.
E-mail addresses: bli@mail.smu.edu (B. Li), zchen@mail.smu.edu (Z. Chen), huan@golem.math.smu.edu (G. Huan).

0309-1708/$ - see front matter © 2004 Elsevier Ltd. All rights reserved.
doi:10.1016/j.advwatres.2003.12.003

are described in detail in Appendices A and B, respectively.

2. The CVFA methods in 3D

As mentioned before, the CVFA methods use non-polynomial function approximations on control volumes. The solution of a linear partial differential equation is approximated with interpolants on these volumes in the solution domain. The approximation solution is then substituted into integration of the differential equation on each control volume to solve for the unknowns at grid points. For more details, refer to [6]. Here we briefly describe the CVFA in three dimensions.

For the purpose of introduction, we consider the model problem

$$\begin{aligned} &-\nabla\cdot(\mathbf{K}(\mathbf{x})\nabla p) = q(\mathbf{x}), \quad \mathbf{x}\in\Omega,\\ &\mathbf{K}(\mathbf{x})\nabla p\cdot\mathbf{n} = g_N(\mathbf{x}), \quad \mathbf{x}\in\Gamma_N,\\ &p = g_D(\mathbf{x}), \quad \mathbf{x}\in\Gamma_D, \end{aligned} \tag{2.1}$$

where $\mathbf{K}$ is a bounded tensor, $\Gamma=\Gamma_N\cup\Gamma_D$ is the boundary of $\Omega\subset\Re^3$, $\Gamma_N\cap\Gamma_D=\emptyset$, q and g_N are integrable functions on Ω and Γ_N, respectively, g_D is bounded on Γ_D, and $\mathbf{n}$ is the outward unit normal to Γ. Note that in the pure Neumann case, the solution p to (2.1) is unique up to an additive constant, and q and g_N need to satisfy the compatibility condition

$$\int_\Omega q\,\mathrm{d}\mathbf{x}+\int_\Gamma g_N\,\mathrm{d}A=0.$$

Let T_h be a partition of Ω into a set of (open) control volumes V_i:

$$\overline{\Omega}=\bigcup_{i=1}^{N}\overline{V}_i, \quad V_i\cap V_j=\emptyset,\ i\neq j,$$

where N is the total number of control volumes and $\overline{\Omega}$ and $\overline{V}_i$ are the closures of Ω and V_i, respectively. These control volumes can be arbitrarily shaped, as seen in Fig. 1. They can be generated from basic tetrahedra, parallelepiped, or prisms; they can also stand alone as the elements of a partition of Ω. We define the boundary of each V_i, as shown in Fig. 2, by

$$\partial V_i=\bigcup_{j=1}^{N_i}e_{ij}, \tag{2.2}$$

where N_i is the number of boundaries of V_i and e_{ij} is the jth boundary adjacent to the jth neighboring control volume of V_i. On each V_i, we integrate the first equation of (2.1) and use the divergence theorem to see that

$$-\int_{\partial V_i}\mathbf{K}\nabla p\cdot\mathbf{n}\,\mathrm{d}A=\int_{V_i}q\,\mathrm{d}\mathbf{x}, \quad i=1,2,\ldots,N, \tag{2.3}$$

where $\mathbf{n}$ is the outward unit normal to ∂V_i. Note that the left-hand side of (2.3) is the flux flowing out of V_i and the right-hand side is the sink in V_i. On each e_{ij}, $j=1,2,\ldots,N_i$, $i=1,2,\ldots,N$, we approximate p by an interpolant p_h:

$$p_h(\mathbf{x})=\sum_{k=0}^{R_{ij}}p^i_{j,k}\phi^i_{j,k}(\mathbf{x}), \quad \mathbf{x}\in e_{ij},\ \ i=1,2,\ldots,N, \tag{2.4}$$

where $p^i_{j,k}$ is the value of p_h at the interpolation point $\mathbf{x}^i_{j,k}$, $\phi^i_{j,k}$ is a basis function at $\mathbf{x}^i_{j,k}$, and $R_{ij}+1$ is the number of interpolation points. The basis functions $\phi^i_{j,k}$ are assumed to satisfy the property:

$$\phi^i_{j,k}(\mathbf{x})=\begin{cases}1 & \text{at the node } \mathbf{x}^i_{j,k},\\ 0 & \text{at other nodes,}\end{cases}$$

for $k=0,1,\ldots,R_{ij}$, $j=1,2,\ldots,N$ and $i=1,2,\ldots,N$. Also, they are supposed to satisfy the property:

$$\begin{aligned}&\sum_{k=0}^{R_{ij}}\phi^i_{j,k}(\mathbf{x})=1, \quad \mathbf{x}\in e_{ij}, \quad j=1,2,\ldots,N_i,\\ &\quad i=1,2,\ldots,N,\end{aligned} \tag{2.5}$$

which implies that a constant pressure is also represented by (2.4). This property is important in the local mass conservation of the CVFA methods.

We replace p in (2.3) by p_h, i.e., substitute (2.4) into (2.3), and use (2.2) to have

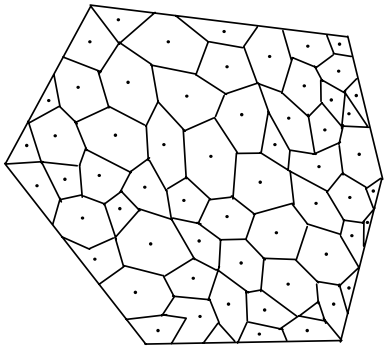

Fig. 1. Cross-sectional view of a partition of domain Ω.

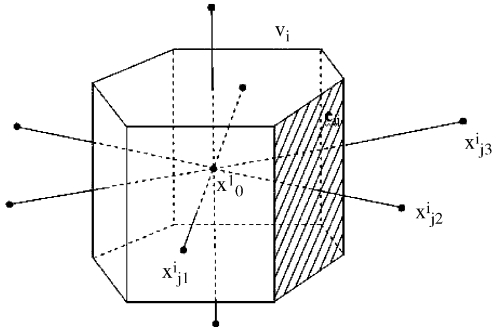

Fig. 2. Control volume V_i.

$$-\sum_{j=1}^{N_i}\sum_{k=0}^{R_{ij}}\left[\int_{e_{ij}}\mathbf{K}(\mathbf{x})\nabla\phi^i_{j,k}(\mathbf{x})\cdot\mathbf{n}\,\mathrm{d}A\right]p^i_{j,k}=\int_{V_i}q\,\mathrm{d}\mathbf{x},\quad i=1,2,\ldots,N. \tag{2.6}$$

Set

$$T^i_{j,k}=-\int_{e_{ij}}\mathbf{K}(\mathbf{x})\nabla\phi^i_{j,k}(\mathbf{x})\cdot\mathbf{n}\,\mathrm{d}A,\quad Q_i=\int_{V_i}q\,\mathrm{d}\mathbf{x}.$$

Then (2.6) becomes

$$\sum_{j=1}^{N_i}\sum_{k=0}^{R_{ij}}T^i_{j,k}p^i_{j,k}=Q_i,\quad i=1,2,\ldots,N. \tag{2.7}$$

This is a linear system for the unknowns $p^i_{j,k}$ at nodes $\mathbf{x}^i_{j,k}$. Using (2.5), the coefficient $T^i_{j,k}$ have a self-illustrated property, i.e.,

$$\sum_{k=0}^{R_{ij}}T^i_{j,k}=0,\quad j=1,2,\ldots,N_i,\ \ i=1,2,\ldots,N. \tag{2.8}$$

Also, Eq. (2.6) implies the continuity of the flux at the interface e_{ij}. If $e_{ij}\subset\Gamma_N$ in (2.6), then the flux on this edge is given by g_N; if, $e_{ij}\subset\Gamma_D$ then the pressure in (2.7) on this edge is given by g_D. A Robin boundary condition (third or mixed type) can also be easily incorporated into (2.6). Finally, by (2.3) and (2.5), we see that the CVFA methods conserve mass on each control volume.

To reduce approximation errors, we should select suitable points in the domain Ω, as the interpolation points $\mathbf{x}^i_{j,k}$. These interpolation points for an interpolant in V_i should be close to V_i as much as possible. In practice, the centroid $\mathbf{x}^i_0$ of V_i and the centroid of the jth neighboring volume of V_i can be chosen as the interpolation points on e_{ij}, for example.

The FD, perpendicular bisection (PEBI) [4], and CVFE methods can be treated as the special cases of the CVFA methods. If all control volumes are rectangular parallelepipeds, only two interpolation points on each face of a control volume, which are the centroids of rectangular parallelepipeds, are used, and linear interpolations are utilized to approximate the solution on faces, then a CVFA method becomes the FD method. Similarly, if only two interpolation points are employed for each face of a control volume and the control volumes have local orthogonality, a CVFA method reduces to the PEBI method. Finally, if the control volumes are constructed from the triangles or tetrahedra and the interpolants are based on piecewise linear polynomials, a CVFA method becomes a CVFE method.

As noted, the interpolation in the CVFA methods exploits non-polynomial functions, so that it does not have any requirement on local orthogonality of control volumes and can be applied to arbitrarily shaped volumes. The CVFA methods are particularly suitable for hybrid grid reservoir simulation. Therefore, they can deal with complicated geometrical and geological features of reservoirs.

As examples, we present two kinds of basis functions $\phi^i_{j,k}$, $k=0,1,\ldots,R_{i,j}$, $j=1,2,\ldots,N_i$, $i=1,2,\ldots,N$. These are the extensions of those in two-dimensional space to three-dimensional space.

The first kind is based on spline interpolants:

$$\omega^i_{j,k}(\mathbf{x})=a^i_{j,k}+b^i_{j,k}x_1+c^i_{j,k}x_2+d^i_{j,k}x_3+\sum_{l=0}^{R_{ij}}f^i_{j,k,l}h^i_{j,k,l}(\mathbf{x}),\quad \mathbf{x}=(x_1,x_2,x_3)\in e_{ij}, \tag{2.9}$$

where $a^i_{j,k},\ b^i_{j,k},\ c^i_{j,k},\ f^i_{j,k,l}\in\Re,\ h^i_{j,k,l}(\mathbf{x})=2(r^i_{j,k,l})^2\ln r^i_{j,k,l}$, and

$$r^i_{j,k,l}(x_1,x_2,x_3)=((x_1-x^i_{1,j,l})^2+(x_2-x^i_{2,j,l})^2+(x_2-x^i_{3,j,l})^2)^{1/2},$$

with $\mathbf{x}^i_{j,l}=(x^i_{1,j,l},x^i_{2,j,l},x^i_{3,j,l})$ being the node coordinates, $k,l=0,1,\ldots,R_{ij}$, $j=1,2,\ldots,N_i$, $i=1,2,\ldots,N$. These spline functions are required to satisfy these properties:

- nodal values:

$$\omega^i_{j,k}(\mathbf{x})=\begin{cases}1 & \text{at the node } \mathbf{x}^i_{j,k},\\ 0 & \text{at other nodes,}\end{cases}$$

- zero total force:

$$\sum_{l=0}^{R_{ij}}f^i_{j,k,l}=0,$$

- and zero total force moment:

$$\sum_{l=0}^{R_{ij}}f^i_{j,k,l}\mathbf{x}^i_{j,l}=0.$$

These three constraints can be used to determine the coefficients $a^i_{j,k}$, $b^i_{j,k}$, $c^i_{j,k}$, $d^i_{j,k}$, and $f^i_{j,k,l}$ associated with $\mathbf{x}^i_{j,k}$ [6]. Now, the basis functions $\phi^i_{j,k}$ are defined by

$$\phi^i_{j,k}(\mathbf{x})=\frac{\omega^i_{j,k}(\mathbf{x})}{\sum_{l=0}^{R_{ij}}\omega^i_{j,l}(\mathbf{x})},\quad \mathbf{x}\in e_{ij}.$$

The second kind of basis functions is based on 'bilinear' interpolants and on control volumes of prismatic type; see Fig. 3. Consider a face e_{i1} of a control volume V_i with centroid $\mathbf{x}_i$. The value of p_h at any point $\mathbf{x}$ on e_{i1} can be obtained by its values at the nodes $\mathbf{x}_i$, $\mathbf{x}^i_1$, $\mathbf{x}^i_2$, and $\mathbf{x}^i_3$, as shown in Fig. 3. The three latter nodes are the centroids of the control volumes adjacent to V_i. Introduce points $\mathbf{x}^i_{1i}$ and $\mathbf{x}^i_{23}$ which lie on the line segments $\mathbf{x}^i_1\mathbf{x}_i$ and $\mathbf{x}^i_2\mathbf{x}^i_3$, respectively, and satisfy

$$\frac{|\mathbf{x}^i_1-\mathbf{x}^i_{1i}|}{|\mathbf{x}_i-\mathbf{x}^i_{1i}|}=\frac{|\mathbf{x}^i_2-\mathbf{x}^i_{23}|}{|\mathbf{x}^i_3-\mathbf{x}^i_{23}|},$$

where $|\cdot|$ indicates the distance. The values at $\mathbf{x}^i_{1i}$ and $\mathbf{x}^i_{23}$ are obtained by 'linear' interpolation:

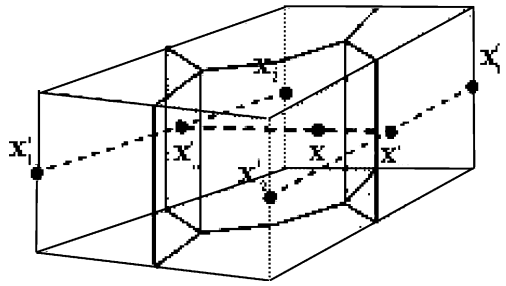

Fig. 3. A bilinear interpolant.

$$p^i(\mathbf{x}^i_{1i}) = p^i(\mathbf{x}^i_1) + \frac{|\mathbf{x}^i_{1i} - \mathbf{x}^i_1|}{|\mathbf{x}_i - \mathbf{x}^i_1|}(p^i(\mathbf{x}_i) - p^i(\mathbf{x}^i_1)),$$

$$p^i(\mathbf{x}^i_{23}) = p^i(\mathbf{x}^i_2) + \frac{|\mathbf{x}^i_{23} - \mathbf{x}^i_2|}{|\mathbf{x}^i_3 - \mathbf{x}^i_2|}(p^i(\mathbf{x}^i_3) - p^i(\mathbf{x}^i_2)),$$

Now, applying the 'linear' interpolation again, the value of p at $\mathbf{x}$ is found by

$$\begin{aligned} p^i_{1,h}(\mathbf{x}) &= p^i(\mathbf{x}^i_{1i}) + \frac{|\mathbf{x} - \mathbf{x}^i_{1i}|}{|\mathbf{x}^i_{23} - \mathbf{x}^i_{1i}|}(p^i(\mathbf{x}^i_{23}) - p^i(\mathbf{x}^i_{1i})) \\ &= \sum_{k=0}^{3} \phi^i_{1,k} p^i_k, \end{aligned} \tag{2.10}$$

where $p^i_0 = p^i(\mathbf{x}_i)$ and

$$\phi^i_{1,0} = \frac{|\mathbf{x}^i_{1i} - \mathbf{x}^i_1|}{|\mathbf{x}_i - \mathbf{x}^i_{1i}|}\left(1 - \frac{|\mathbf{x} - \mathbf{x}^i_{1i}|}{|\mathbf{x}^i_{23} - \mathbf{x}^i_{1i}|}\right),$$

$$\phi^i_{1,1} = \left(1 - \frac{|\mathbf{x}^i_{1i} - \mathbf{x}^i_1|}{|\mathbf{x}_i - \mathbf{x}^i_1|}\right)\left(1 - \frac{|\mathbf{x} - \mathbf{x}^i_{1i}|}{|\mathbf{x}^i_{23} - \mathbf{x}^i_{1i}|}\right),$$

$$\phi^i_{1,2} = \left(1 - \frac{|\mathbf{x}^i_{23} - \mathbf{x}^i_2|}{|\mathbf{x}^i_3 - \mathbf{x}^i_2|}\right)\frac{|\mathbf{x} - \mathbf{x}^i_{1i}|}{|\mathbf{x}^i_{23} - \mathbf{x}^i_{1i}|},$$

$$\phi^i_{1,3} = \frac{|\mathbf{x}^i_{23} - \mathbf{x}^i_2|}{|\mathbf{x}^i_3 - \mathbf{x}^i_2|} \cdot \frac{|\mathbf{x} - \mathbf{x}^i_{1i}|}{|\mathbf{x}^i_{23} - \mathbf{x}^i_{1i}|}.$$

Representation (2.10) can be extended to other faces e_{ij} of V_i:

$$p^i_{j,h}(\mathbf{x}) = \sum_{k=0}^{3} \phi^i_{j,k} p^i_{k+j-1}, \quad j = 2, 3, \ldots, N_i.$$

For a nonlinear differential equation system, the CVFA methods cannot be directly used to solve it. But we can use the Newton–Raphson method to linearize the nonlinear partial differential equation system and obtain the iterative equation systems for it first. Then we apply the CVFA methods to discretizing the iterative equations and solve them.

It is assumed that a general nonlinear differential equation system has the form

$$\pounds_m\{F_m[\mathbf{p}(\mathbf{x})]\} = f_m(\mathbf{x}), \quad m = 1, 2, \ldots, M, \quad \mathbf{x} \in \Omega, \tag{2.11}$$

where $\pounds_m$ denotes a linear differential operator, $F_m(\cdot)$ is a nonlinear function, $\mathbf{p}$ is the vector of continuous dependent variables, $\mathbf{p} = [p_1, p_2, \ldots, p_M]^t$, $\mathbf{f}$ is a vector of continuous functions, $\mathbf{f} = [f_1, f_2, \ldots, f_M]^t$ and M is the total number of equations.

We apply the Newton–Raphson method to establish the iterative equation system for solving (2.11). Taylor's series expansion for $F_m(\mathbf{p} + \delta\mathbf{p})$ is

$$F_m(\mathbf{p} + \delta\mathbf{p}) = F_m(\mathbf{p}) + \nabla F_m(\mathbf{p}) \cdot \delta\mathbf{p} + \mathcal{O}(\delta\mathbf{p}^2). \tag{2.12}$$

If the high order term $\mathcal{O}(\delta\mathbf{p}^2)$ is truncated, $F_m(\mathbf{p} + \delta\mathbf{p})$ can be approximated by

$$F_m(\mathbf{p} + \delta\mathbf{p}) \approx F_m(\mathbf{p}) + \nabla F_m(\mathbf{p}) \cdot \delta\mathbf{p}. \tag{2.13}$$

If we substitute (2.13) into (2.11), we obtain the iterative equations

$$\begin{aligned} &\pounds_m[F_m(\mathbf{p}_l) + \nabla F_m(\mathbf{p}_l) \cdot \delta\mathbf{p}_l] = f_m(\mathbf{x}), \\ &\quad m = 1, 2, \ldots, M, \quad \mathbf{x} \in \Omega, \end{aligned} \tag{2.14}$$

where $\mathbf{p}_l$ is the lth iterative solution of $\mathbf{p}$ and $\nabla F_m(\mathbf{p_l})$ is $\nabla F_m(\mathbf{p})$ for $\mathbf{p} = \mathbf{p}_l$, with the initial iterative solution $\mathbf{p}_0$. In the iterative equation system (2.14), the correction vector $\delta\mathbf{p}_l$ is taken as the unknown to be solved for. This equation system can be rewritten into

$$\nabla F_m(\mathbf{p}_l) \cdot \pounds_m(\delta\mathbf{p}_l) = g_m(\mathbf{x}), \quad m = 1, 2, \ldots, M, \quad \mathbf{x} \in \Omega, \tag{2.15}$$

where $g_m(\mathbf{x}) = f_m(\mathbf{x}) - \pounds_m[F_m(\mathbf{p}_l)]$, since $F_m(\mathbf{p_l})$ and $\nabla F_m(\mathbf{p_l})$ are treated as fixed. Now, (2.15) is a linear system for $\delta\mathbf{p}_l$, and the CVFA methods can be applied to it.

The new solution vector $\mathbf{p}_{l+1}$ can be obtained by adding the correction vector $\delta\mathbf{p}_l$ to the previous iterative solution vector $\mathbf{p}_l$; i.e.,

$$\mathbf{p}_{l+1} = \mathbf{p}_l + \delta\mathbf{p}_l. \tag{2.16}$$

This iteration process proceeds until the Euclidian norm of $\delta\mathbf{p}_l$ is smaller than the prescribed value.

3. Discretization of the black oil model

In the black oil model, it is assumed that no mass transfer occurs between the water phase and the other two phases, i.e., gas and oil. In the hydrocarbon system, only two components are present. The 'oil' component is the residual liquid at atmospheric pressure left after a differential vaporization, while the 'gas' component is the remaining fluid.

Let ϕ and K denote the porosity and permeability of a porous medium $\Omega \subset \Re^3$, s_α, μ_α, p_α, $\mathbf{u}_\alpha$, B_α, and $K_{r\alpha}$ be the saturation, viscosity, pressure, volumetric velocity,

formation volume factor, and relative permeability of the α phase, $\alpha = \mathrm{w}, \mathrm{o}, \mathrm{g}$, respectively, and R_{so} be the gas solubility. Then the mass conservation equations of the black oil model are [1]

$$-\nabla \cdot \left(\frac{\rho_{\mathrm{WS}}}{B_{\mathrm{w}}} \mathbf{u}_{\mathbf{w}} \right) + q_{\mathrm{w}} = \frac{\partial}{\partial t} \left(\phi \frac{\rho_{\mathrm{WS}}}{B_{\mathrm{w}}} s_{\mathrm{w}} \right) \tag{3.1}$$

for the water component,

$$-\nabla \cdot \left(\frac{\rho_{\mathrm{OS}}}{B_{\mathrm{o}}} \mathbf{u}_{\mathbf{o}} \right) + q_{\mathrm{o}} = \frac{\partial}{\partial t} \left(\phi \frac{\rho_{\mathrm{OS}}}{B_{\mathrm{o}}} s_{\mathrm{o}} \right) \tag{3.2}$$

for the oil component,

$$-\nabla \cdot \left(\frac{\rho_{\mathrm{GS}}}{B_{\mathrm{g}}} \mathbf{u}_{\mathbf{g}} + \frac{R_{\mathrm{so}} \rho_{\mathrm{GS}}}{B_{\mathrm{o}}} \mathbf{u}_{\mathbf{o}} \right) + q_{\mathrm{g}} = \frac{\partial}{\partial t} \left[\phi \left(\frac{\rho_{\mathrm{GS}}}{B_{\mathrm{g}}} s_{\mathrm{g}} + \frac{R_{\mathrm{so}} \rho_{\mathrm{GS}}}{B_{\mathrm{o}}} s_{\mathrm{o}} \right) \right] \tag{3.3}$$

for the gas component, where $\rho_{\beta \mathrm{S}}$ is the density of the β component at standard conditions (stock tank), $\beta = \mathrm{W}, \mathrm{O}, \mathrm{G}$, q_α is the mass flow rate of the a phase at wells,

$$q_{\mathrm{g}} = q_{\mathrm{g}}^{\mathrm{G}} + q_{\mathrm{o}}^{\mathrm{G}}.$$

The volumetric velocity of the α phase is represented by Darcy's law

$$\mathbf{u}_\alpha = -\frac{K K_{r\alpha}}{\mu_\alpha} \nabla \Phi_\alpha, \quad \alpha = \mathrm{g}, \mathrm{o}, \mathrm{w}, \tag{3.4}$$

where the potential Φ_α of the α phase is given by

$$\Phi_\alpha = p_\alpha - \rho_\alpha \tilde{g} D, \quad \alpha = \mathrm{w}, \mathrm{o}, \mathrm{g}, \tag{3.5}$$

ρ_α represents the density of the α phase, $\tilde{g}$ is the gravitational constant, and D is the depth function. The saturations of the water, oil, and gas phases satisfy the constraint

$$s_{\mathrm{w}} + s_{\mathrm{o}} + s_{\mathrm{g}} = 1. \tag{3.6}$$

Furthermore, the phase pressures are related by the capillary pressures p_{cow} and p_{cgo}:

$$p_{\mathrm{cow}} = p_{\mathrm{o}} - p_{\mathrm{w}}, \quad p_{\mathrm{cgo}} = p_{\mathrm{g}} - p_{\mathrm{o}}. \tag{3.7}$$

Finally, the mass flow rates of wells are given by Peaceman's formulas [10]

$$\begin{aligned}
q_{\mathrm{o}} &= \sum_{k=1}^{N_{\mathrm{w}}} \sum_{m=1}^{M_{wk}} = \frac{2\pi \Delta z_{k,m}}{\ln(r_{e,k}/r_{c,k}) + s_{k,m}} \frac{K K_{r\mathrm{o}} \rho_{\mathrm{OS}}}{\mu_{\mathrm{o}} B_{\mathrm{o}}} \\
&\quad \times [p_{\mathrm{bh},k} - p_{\mathrm{o}} - \rho_{\mathrm{o}} \tilde{g}(D_{\mathrm{w},k} - D)] \delta_{k,m}, \\
q_{\mathrm{w}} &= \sum_{k=1}^{N_{\mathrm{w}}} \sum_{m=1}^{M_{wk}} = \frac{2\pi \Delta z_{k,m}}{\ln(r_{e,k}/r_{c,k}) + s_{k,m}} \frac{K K_{r\mathrm{w}} \rho_{\mathrm{WS}}}{\mu_{\mathrm{w}} B_{\mathrm{w}}} \\
&\quad \times [p_{\mathrm{bh},k} - p_{\mathrm{w}} - \rho_{\mathrm{w}} \tilde{g}(D_{\mathrm{w},k} - D)] \delta_{k,m}, \\
q_{\mathrm{g}}^{\mathrm{G}} &= \sum_{k=1}^{N_{\mathrm{w}}} \sum_{m=1}^{M_{wk}} = \frac{2\pi \Delta z_{k,m}}{\ln(r_{e,k}/r_{c,k}) + s_{k,m}} \frac{K K_{r\mathrm{g}} \rho_{\mathrm{GS}}}{\mu_{\mathrm{g}} B_{\mathrm{g}}} \\
&\quad \times [p_{\mathrm{bh},k} - p_{\mathrm{g}} - \rho_{\mathrm{g}} \tilde{g}(D_{\mathrm{w},k} - D)] \delta_{k,m}, \\
q_{\mathrm{o}}^{\mathrm{G}} &= \sum_{k=1}^{N_{\mathrm{w}}} \sum_{m=1}^{M_{wk}} = \frac{2\pi \Delta z_{k,m}}{\ln(r_{e,k}/r_{c,k}) + s_{k,m}} \frac{K K_{r\mathrm{o}} R_{\mathrm{so}} \rho_{\mathrm{GS}}}{\mu_{\mathrm{o}} B_{\mathrm{o}}} \\
&\quad \times [p_{\mathrm{bh},k} - p_{\mathrm{o}} - \rho_{\mathrm{o}} \tilde{g}(D_{\mathrm{w},k} - D)] \delta_{k,m},
\end{aligned} \tag{3.8}$$

where $\delta_{k,m} = \delta(\mathbf{x} - \mathbf{x}_{k,m})$ (the Dirac delta function at $\mathbf{x}_{k,m}$), N_{w} is the total number of wells, $M_{\mathrm{w},k}$ is the total number of perforated zones of the kth well, $s_{k,m}$, $\Delta z_{k,m}$ and $\mathbf{x}_{k,m}$ are the skin factor, segment length, and central location of the mth perforated zone of the kth well, $r_{c,k}$ and $r_{e,k,m}$ are the wellbore and drainage radii of the kth well at the grid block in which $\mathbf{x}_{k,m}$ is located, respectively, and $p_{\mathrm{bh},k}$ is the bottom hole pressure of the kth well at datum $D_{\mathrm{w},k}$.

The model is completed by specifying boundary and initial conditions. In this paper we consider no flow boundary conditions

$$\mathbf{u}_\alpha \cdot \mathbf{n} = 0, \quad \alpha = \mathrm{w}, \mathrm{o}, \mathrm{g}, \quad \mathbf{x} \in \partial\Omega, \tag{3.9}$$

where $\mathbf{n}$ is the outward unit norm to the boundary $\partial\Omega$ of the reservoir domain Ω. The initial conditions depend on the state of a reservoir. When all gas dissolves into the oil phase, there is no gas phase present, i.e., $s_{\mathrm{g}} = 0$. In such a case, the reservoir is called at the undersaturated state. If all three phases co-exist, the reservoir is referred to as at the saturated state. The critical point where three-phase flow becomes two-phase flow or vice versa is called the bubble point [2], and the pressure of a reservoir at this point is the bubble point pressure. At the undersaturated state, we use $p = p_{\mathrm{o}}, s_{\mathrm{w}}$, and p_{b} as the unknowns, where p_{b} is the bubble point pressure; see Appendix A. The corresponding initial conditions are

$$\begin{aligned}
&p(\mathbf{x}, 0) = p^0(\mathbf{x}), \quad \mathbf{x} \in \Omega, \\
&p_{\mathrm{b}}(\mathbf{x}, 0) = p_{\mathrm{b}}^0(\mathbf{x}), \quad \mathbf{x} \in \Omega, \\
&s_{\mathrm{w}}(\mathbf{x}, 0) = s_{\mathrm{w}}^0(\mathbf{x}), \quad \mathbf{x} \in \Omega.
\end{aligned} \tag{3.10}$$

At the saturated state, we employ $p = p_0$, s_{w}, and s_{o} as the unknowns. In this case, the initial conditions become

$$p(\mathbf{x},0)=p^0(\mathbf{x}),\quad \mathbf{x}\in\Omega,$$
$$s_{\mathrm{w}}(\mathbf{x},0)=s_{\mathrm{w}}^0(\mathbf{x}),\quad \mathbf{x}\in\Omega, \tag{3.11}$$
$$s_{\mathrm{o}}(\mathbf{x},0)=s_{\mathrm{o}}^0(\mathbf{x}),\quad \mathbf{x}\in\Omega.$$

Various well constraints need to be taken into account. For an injection well, two kinds of well constraints are permitted. They are, respectively, the constant bottom hole pressure and constant injection flow rate. In the former case, the bottom hole pressure is fixed:

$$p_{\mathrm{bh},k}=P_{\mathrm{bh},k}, \tag{3.12}$$

where k is the sequential number of the well which has this kind of well control and $P_{\mathrm{bh},k}$ is the given bottom hole pressure of this well. In the latter case, the injection flow rate controls for water and gas injection wells are, respectively,

$$\begin{aligned} q_{\mathrm{w},k}&=\sum_{m=1}^{M_{\mathrm{w},k}}\int_{V_{k,m}}\mathrm{WI}_{k,m}\frac{K_{r\mathrm{w}\max}\rho_{\mathrm{WS}}}{\mu_{\mathrm{w}}B_{\mathrm{w}}}\\ &\quad\times[p_{\mathrm{bh}}-p_{\mathrm{w}}-\rho_{\mathrm{w}}\tilde{g}(D_{\mathrm{w},k}-D)]\delta_{k,m}\,\mathrm{d}\mathbf{x}=Q_{\mathrm{W},k},\\ q_{\mathrm{g},k}^{\mathrm{G}}&=\sum_{m=1}^{M_{\mathrm{w},k}}\int_{V_{k,m}}\mathrm{WI}_{k,m}\frac{K_{r\mathrm{g}\max}\rho_{\mathrm{GS}}}{\mu_{\mathrm{g}}B_{\mathrm{g}}}\\ &\quad\times[p_{\mathrm{bh}}-p_{\mathrm{g}}-\rho_{\mathrm{g}}\tilde{g}(D_{\mathrm{w},k}-D)]\delta_{k,m}\,\mathrm{d}\mathbf{x}=Q_{\mathrm{g},k}^{\mathrm{G}}, \end{aligned} \tag{3.13}$$

where $Q_{\mathrm{W},k}$ and $Q_{\mathrm{g},k}^{\mathrm{G}}$ are the given water and gas injection rates for the water and gas injection rate controls, respectively, $K_{r\alpha\max}$ is the maximum relative permeability of the α phase, $\alpha=\mathrm{w},\mathrm{g}$, $V_{k,m}$ denotes the control volume in which the mth perforated zone of the kth well falls, and the well index $\mathrm{WI}_{k,m}$ is denned as

$$\mathrm{WI}_{k,m}=\frac{2\pi\Delta z_{k,m}K}{\ln(r_{e,k}/r_{c,k})+s_{k,m}}.$$

For a production well, the constraints are three kinds: a constant bottom hole pressure, a constant total flow rate, and a constant total liquid production rate. The constant bottom hole pressure takes the same form as (3.12). For an oil production well, the oil production rate control is

$$\begin{aligned} q_{\mathrm{o},k}&=\sum_{m=1}^{M_{\mathrm{w},k}}\int_{V_{k,m}}\mathrm{WI}_{k,m}\frac{K_{r\mathrm{o}}\rho_{\mathrm{OS}}}{\mu_{\mathrm{o}}B_{\mathrm{o}}}\\ &\quad\times[p_{\mathrm{bh}}-p_{\mathrm{o}}-\rho_{\mathrm{o}}\tilde{g}(D_{\mathrm{w},k}-D)]\delta_{k,m}\,\mathrm{d}\mathbf{x}=Q_{\mathrm{O},k}, \end{aligned} \tag{3.14}$$

where $Q_{\mathrm{O},k}$ is the given oil production rate, which is the volume of produced oil per day. For a gas production well, the production rate control is

$$\begin{aligned} q_{\mathrm{g},k}^{\mathrm{G}}+q_{\mathrm{o},k}^{\mathrm{G}}&=\sum_{m=1}^{M_{\mathrm{w},k}}\int_{V_{k,m}}\mathrm{WI}_{k,m}\frac{K_{r\mathrm{g}}\rho_{\mathrm{GS}}}{\mu_{\mathrm{g}}B_{\mathrm{g}}}\\ &\quad\times[p_{\mathrm{bh}}-p_{\mathrm{g}}-\rho_{\mathrm{g}}\tilde{g}(D_{\mathrm{w},k}-D)]\delta_{k,m}\,\mathrm{d}\mathbf{x}\\ &\quad+\sum_{m=1}^{M_{\mathrm{w},k}}\int_{V_{k,m}}\mathrm{WI}_{k,m}\frac{K_{r\mathrm{o}}R_{\mathrm{so}}\rho_{\mathrm{GS}}}{\mu_{\mathrm{o}}B_{\mathrm{o}}}\\ &\quad\times[p_{\mathrm{bh}}-p_{\mathrm{o}}-\rho_{\mathrm{o}}\tilde{g}(D_{\mathrm{w},k}-D)]\delta_{k,m}\,\mathrm{d}\mathbf{x}=Q_k^{\mathrm{G}}, \end{aligned} \tag{3.15}$$

where Q_k^{G} is the given gas production rate of the kth well. Note that the gas–oil ratio (GOR), which is the ratio of the gas production rate to the oil production rate, at a perforated zone of a well must be less than a certain limit; over this limit, that perforated zone needs to be shut down. The liquid flow rate control is only applicable for an oil production well and is of the form

$$\begin{aligned} q_{l,k}&=\sum_{m=1}^{M_{\mathrm{w},k}}\int_{V_{k,m}}\mathrm{WI}_{k,m}\frac{K_{r\mathrm{w}}\rho_{\mathrm{WS}}}{\mu_{\mathrm{w}}B_{\mathrm{w}}}\\ &\quad\times[p_{\mathrm{bh}}-p_{\mathrm{w}}-\rho_{\mathrm{w}}\tilde{g}(D_{\mathrm{w},k}-D)]\delta_{k,m}\,\mathrm{d}\mathbf{x}\\ &\quad+\sum_{m=1}^{M_{\mathrm{w},k}}\int_{V_{k,m}}\mathrm{WI}_{k,m}\frac{K_{r\mathrm{o}}\rho_{\mathrm{OS}}}{\mu_{\mathrm{o}}B_{\mathrm{o}}}\\ &\quad\times[p_{\mathrm{bh}}-p_{\mathrm{o}}-\rho_{\mathrm{o}}\tilde{g}(D_{\mathrm{w},k}-D)]\delta_{k,m}\,\mathrm{d}\mathbf{x}=Q_{\mathrm{L},k}, \end{aligned} \tag{3.16}$$

where $Q_{\mathrm{L},k}$ is the given total liquid production rate of the kth well. Also, the water cut, which is the ratio of the water production rate and the total liquid production rate, at a perforated zone of a well with this kind of well constraint must be less than a certain limit; otherwise, that perforated zone needs to be shut down.

We use the fully implicit technique to solve the above nonlinear equations and apply the CVFA methods to discretize them in space. To model accurately the geometrical and geological features of a reservoir, a hybrid grid needs to be used for reservoir simulation. Since the CVFA methods can directly discretize an equation on an arbitrarily shaped grid and are especially suitable for the hybrid grid reservoir simulation, we apply these methods to dealing with the discretization of the governing equations of the black oil model and the treatment of wells. We very briefly review the discretization of the black oil model using the CVFA and the linearization of this model using Newton–Raphson's procedure. For more details, refer to Appendices A and B. The fluid flow at a location in a reservoir may be two phase, three phase, or at the bubble point state. For different states, the unknowns will be different, as noted. For example, at the saturated state, there is free gas, the gas saturation will be an unknown, and the bubble point pressure is equal to the reservoir pressure. On the other hand, at the undersaturated state, there will be no free gas; i.e., the gas saturation will be zero, and the bubble

point pressure will be different from the reservoir pressure. Therefore, the selection of the unknowns should be corresponding to the states of a reservoir. The integral forms of the governing equations on each control volume are solved to honor the mass conservation property. For the undersaturated state, the lth iteration values of the water and oil potentials on boundary e_{ij} of a control volume V_i at the $(n+1)$th time step are approximated by

$$\begin{aligned}(\Phi_{\mathrm{wh}})_l^{(n+1)} &= \sum_{r=0}^{R_{ij}} (\Phi^i_{\mathrm{w}j,r})_l^{(n+1)} \phi^i_{j,r}(\mathbf{x}), \quad \mathbf{x} \in e_{ij},\\ (\Phi_{\mathrm{oh}})_l^{(n+1)} &= \sum_{r=0}^{R_{ij}} (\Phi^i_{\mathrm{o}j,r})_l^{(n+1)} \phi^i_{j,r}(\mathbf{x}), \quad \mathbf{x} \in e_{ij},\end{aligned} \tag{3.17}$$

where l refers to the iteration number of Newton–Raphson's iterations, $\phi^i_{j,r}(\mathbf{x})$, $r = 0, 1, \ldots, R_{i,j}$, are the shape functions, $R_{ij}+1$ is the total number of interpolation points for $(\Phi_{\alpha h})_l^{(n+1)}$ on e_{ij}, and $(\Phi^i_{\alpha j,r})_l^{(n+1)}$ denotes the nodal value of $(\Phi_{\alpha h})_l^{(n+1)}$, $\alpha = w, o$ (see Section 2). Since δp, δp_{b}, and δs_{w} at grid points in all time steps need to be obtained for this state, we approximate the lth iteration values of these variables at the $(n+1)$th time step by

$$\begin{aligned}(\delta p_h)_l^{(n+1)} &= \sum_{r=0}^{R_{ij}} \left(\delta p^i_{j,r}\right)_l^{(n+1)} \phi^i_{j,r}(\mathbf{x}), \quad \mathbf{x} \in e_{ij},\\ (\delta s_{\mathrm{wh}})_l^{(n+1)} &= \sum_{r=0}^{R_{ij}} \left(\delta s^i_{\mathrm{w}j,r}\right)_l^{(n+1)} \phi^i_{j,r}(\mathbf{x}), \quad \mathbf{x} \in e_{ij},\\ (\delta p_{\mathrm{bh}})_l^{(n+1)} &= \sum_{r=0}^{R_{ij}} \left(\delta p^i_{b_{j,r}}\right)_l^{(n+1)} \phi^i_{j,r}(\mathbf{x}), \quad \mathbf{x} \in e_{ij}.\end{aligned} \tag{3.18}$$

We substitute these interpolants into the linearized governing equations given in Appendix A.1 to obtain the discrete equations, which are given in Appendix B.1. In these discrete equations, the lth iteration values of increments $(\delta p^i_{j,r})_l^{(n+1)}$, $(\delta s^i_{\mathrm{w}j,r})_l^{(n+1)}$, and $(\delta p^i_{b_{j,r}})_l^{(n+1)}$ at the $(n+1)$th time step at nodes $\mathbf{x}^i_{j,r}$ are the unknowns to be solved for. For a well with a flow rate control, the increment of its bottom hole pressure also needs to be obtained. After these increments are obtained, the iteration solutions at grid point $\mathbf{x}_i$ and the bottom hole pressure of the kth well are updated by

$$\begin{aligned}(p_i)_{l+1}^{(n+1)} &= (p_i)_l^{(n+1)} + (\delta p_i)_l^{(n+1)},\\ (s_{\mathrm{w}i})_{l+1}^{(n+1)} &= (s_{\mathrm{w}i})_l^{(n+1)} + (\delta s_{\mathrm{w}i})_l^{(n+1)},\\ (p_{b_i})_{l+1}^{(n+1)} &= (p_{b_i})_l^{(n+1)} + (\delta p_{b_i})_l^{(n+1)},\\ (p_{\mathrm{bh},k})_{l+1}^{(n+1)} &= (p_{\mathrm{bh},k})_l^{(n+1)} + (\delta p_{\mathrm{bh},k})_l^{(n+1)}.\end{aligned} \tag{3.19}$$

Similarly, for the saturated state, we approximate the lth iteration values of the water, oil, and gas potentials at the $(n+1)$th time step by

$$\begin{aligned}(\Phi_{\mathrm{wh}})_l^{(n+1)} &= \sum_{r=0}^{R_{ij}} (\Phi^i_{\mathrm{w}j,r})_l^{(n+1)} \phi^i_{j,r}(\mathbf{x}), \quad \mathbf{x} \in e_{ij},\\ (\Phi_{\mathrm{oh}})_l^{(n+1)} &= \sum_{r=0}^{R_{ij}} (\Phi^i_{\mathrm{o}j,r})_l^{(n+1)} \phi^i_{j,r}(\mathbf{x}), \quad \mathbf{x} \in e_{ij},\\ (\Phi_{\mathrm{gh}})_l^{(n+1)} &= \sum_{r=0}^{R_{ij}} (\Phi^i_{\mathrm{g}j,r})_l^{(n+1)} \phi^i_{j,r}(\mathbf{x}), \quad \mathbf{x} \in e_{ij},\end{aligned} \tag{3.20}$$

and approximate the unknowns $(\delta p)_l^{(n+1)}$, $(\delta s_{\mathrm{w}})_l^{(n+1)}$, and $(\delta s_{\mathrm{o}})_l^{(n+1)}$ by

$$\begin{aligned}(\delta p_h)_l^{(n+1)} &= \sum_{r=0}^{R_{ij}} (\delta p^i_{j,r})_l^{(n+1)} \phi^i_{j,r}(\mathbf{x}), \quad \mathbf{x} \in e_{ij},\\ (\delta s_{\mathrm{wh}})_l^{(n+1)} &= \sum_{r=0}^{R_{ij}} (\delta s^i_{\mathrm{w}j,r})_l^{(n+1)} \phi^i_{j,r}(\mathbf{x}), \quad \mathbf{x} \in e_{ij},\\ (\delta s_{\mathrm{oh}})_l^{(n+1)} &= \sum_{r=0}^{R_{ij}} (\delta s^i_{\mathrm{o}j,r})_l^{(n+1)} \phi^i_{j,r}(\mathbf{x}), \quad \mathbf{x} \in e_{ij}.\end{aligned} \tag{3.21}$$

We substitute them into the linearized governing equations in Appendix A.2 to get the discrete equations, which are listed in Appendix B.2. The iteration solution values at grid point $\mathbf{x}_i$ and the kth well, which has a flow rate control, are updated by

$$\begin{aligned}(p_i)_{l+1}^{(n+1)} &= (p_i)_l^{(n+1)} + (\delta p_i)_l^{(n+1)},\\ (s_{\mathrm{w}i})_{l+1}^{(n+1)} &= (s_{\mathrm{w}i})_l^{(n+1)} + (\delta s_{\mathrm{w}i})_l^{(n+1)},\\ (s_{\mathrm{o}i})_{l+1}^{(n+1)} &= (s_{\mathrm{o}i})_l^{(n+1)} + (\delta s_{\mathrm{o}i})_l^{(n+1)},\\ (p_{\mathrm{bh},k})_{l+1}^{(n+1)} &= (p_{\mathrm{bh},k})_l^{(n+1)} + (\delta p_{\mathrm{bh},k})_l^{(n+1)}.\end{aligned} \tag{3.22}$$

Upstream weighting is an important technique in simulating multiphase flow in porous media. Here we briefly discuss how to incorporate this technique into the discretization in space of the mass conservation equations of the black oil model. For the flux and source terms of a control volume on the left-hand side of the linearized and discretized conservation equations given in Appendix B, we use one-point value upstream weighting to determine their mobility factors, which are functions of saturation and pressure. On a face of a control volume, if the flux flows into this volume, the mobility factor of the flux term on this face will take the value at the centroid of the neighboring control volume, which shares this interface; if the flux flows out of this volume on this face, the mobility factor on this face will take the value at the centroid of this control volume. Similarly, for the source term corresponding to a perforated zone of a well, if the flux flows from the wellbore to the reservoir, the mobility factor will take the value at the wellbore, or vice versa. Furthermore, this approach will lead to nonsymmetric coefficient matrices of linear equation systems because some unknowns are part of the mobility factors.

We utilize some practical techniques [5] to control convergences of Newton–Raphson's iterations and the ORTHOMIN iterations [11], which are used to solve the linear equation systems. In this paper we briefly state them. For more details, please refer to [5,7].

To select suitable time steps, from our experimental experiences we have adopted the following empirical rules:

Rule 1. With a given maximum time step $\Delta t_{\max}$ and a given minimum time step $\Delta t_{\min}$, the time step to be determined Δt_{n+1} must satisfy that $\Delta t_{\min} \leqslant \Delta t_{n+1} \leqslant \Delta t_{\max}$.

Rule 2. At the saturated state, Δt_{n+1} is bounded by

$$\Delta t_{n+1} \leqslant \Delta t_n \min\left\{3, \frac{(\mathrm{d}P)_{\max}}{(\delta p)^{(n)}_{\max}}, \frac{(\mathrm{d}S_{\mathrm{w}})_{\max}}{(\delta s_{\mathrm{w}})^{(n)}_{\max}}, \frac{(\mathrm{d}S_{\mathrm{g}})_{\max}}{(\delta s_{\mathrm{g}})^{(n)}_{\max}}\right\}, \tag{3.23}$$

where $(\mathrm{d}P)_{\max}$, $(\mathrm{d}S_{\mathrm{w}})_{\max}$, and $(\mathrm{d}S_{\mathrm{g}})_{\max}$ are the allowable maximum values of the pressure, water saturation, and gas saturation increments, respectively, and $(\delta p)^{(n)}_{\max}$, $(\delta s_{\mathrm{w}})^{(n)}_{\max}$, $(\delta s_{\mathrm{g}})^{(n)}_{\max}$ are the maximum values of these increments at the nth time step. At the undersaturated state, (3.23) becomes

$$\Delta t_{n+1} \leqslant \Delta t_n \min\left\{3, \frac{(\mathrm{d}P)_{\max}}{(\delta p)^{(n)}_{\max}}, \frac{(\mathrm{d}S_{\mathrm{w}})_{\max}}{(\delta s_{\mathrm{w}})^{(n)}_{\max}}, \frac{(\mathrm{d}P_{\mathrm{b}})_{\max}}{(\delta p_{\mathrm{b}})^{(n)}_{\max}}\right\}, \tag{3.24}$$

where $(\mathrm{d}P_{\mathrm{b}})_{\max}$ is the allowable maximum value of the bubble point pressure increment.

Rule 3. Δt_{n+1} should guarantee that the simulation time can reach the given period times.

With these rules, the time steps can be automatically selected. The choice of Δt_{n+1} also needs to take into account convergence of Newton–Raphson's iterations. If the number of Newton–Raphson's iterations is greater than an allowable maximum iteration number with Δt_{n+1} selected by Rules 1–3, the determined time step may be too large and it needs to be reduced. We first cut Δt_{n+1} by $\Delta t_{n+1}/3$. Then the oil phase pressure, bubble point pressure, water saturation, and oil saturation at the nth time step are taken as the first iteration values of Newton–Raphson's iterations at the $(n+1)$th time step.

To terminate a Newton–Raphson iteration process, some important factors must be considered. First, the iteration number must be greater than a given minimum number and smaller than a given maximum number. Second, the iteration values of the unknowns and the right-hand vectors of the linear equation systems to be solved are also used as part of the termination condition. The absolute iteration values of the increments of pressure, water saturation, oil saturation or bubble point pressure pressure, and the bottom hole pressures of wells have to be less than their respective allowable maximum limits. Also, the ratio of the infinite norm of the right-hand side vector of an LES to the maximum absolute value of the sum of the oil and gas component flow rates of perforated zones of wells have to be less than a certain given limit.

To terminate the ORTHOMIN iterations [11], we employ the maximum allowable iteration number and the ratio of the norm of the residual error vector $\mathbf{r}_k$ of a linear equation system to the norm of its right-hand side vector $\mathbf{b}$ as the termination conditions of these iterations.

4. Numerical experiments

We use the benchmark problems of the first and second comparative solution projects (CSP) of the SPE to check: (a) the validity of the CVFA methods to discretize the governing equation of the black oil model, (b) their grid orientation effects, (c) stability and convergence of these methods to deal with a 'bubble point' problem and a three-phase coning problem, and (d) computational costs of the CVFA methods when a flexible grid is used. Due to a layer structure in the vertical direction of the reservoirs under consideration, a simple FD method is used in the x_3-direction. When we refer to the 5-point FD method below, we mean this method in the x_1x_2-plane; in the x_3-direction, two more points are added, so in fact it is the 7-point FD method in three dimensions. When we state the 9-point FD method below, again we mean this method in the horizontal direction; in the vertical direction, two more points are added.

4.1. Gas displacement

This simulation problem is chosen from the second case of the benchmark problem of the first CSP [8]. This benchmark problem is a challenging problem in reservoir simulation. It was designed to test the stability of black oil reservoir simulators to deal with the strong nonlinearity of the governing equations and the 'crossing bubble point' problem. At the saturated state of a reservoir, the free gas exits and its relatively high compressibility leads to the strong nonlinearity of these equations [7]. Also, as noted, a location in a reservoir may change from two phase to three phase, or vice versa; when Newton–Raphson's linearization method is applied to solving these equations, the selection of the unknowns depends on the states. Locating the bubble point is very important because it determines convergence of Newton–Raphson's iterations.

A grid of rectangular parallelepipeds, which consists of 300 grid blocks, for the reservoir under consideration is given in Fig. 4. The diagonal cross-sectional view of this reservoir can be seen in Fig. 5.

Here we briefly state the physical data; for more details on these data, see [8]. At the initial state, the reservoir reaches equilibrium with initial reservoir pressure 4800 psia at 8400 ft and with reservoir temperature 200 F. The depth to the top of this reservoir is 8325 ft. The gas/oil contact and water/oil contact, respectively, locate at 8320 and 8450 ft. The capillary pressure is zero. The reservoir porosity measured at a pressure of 14.7 psia is 0.3. The rock compressibility is 3×10^{-6} 1/psi. The PVT function data for oil, water, and gas are, respectively, given in Tables 1–5, where FVF stands for the formation volume factor. The horizontal and vertical absolute permeability distribution and the initial water and oil saturation distribution are indicated in Fig. 5. The saturation function data are listed in Table 6.

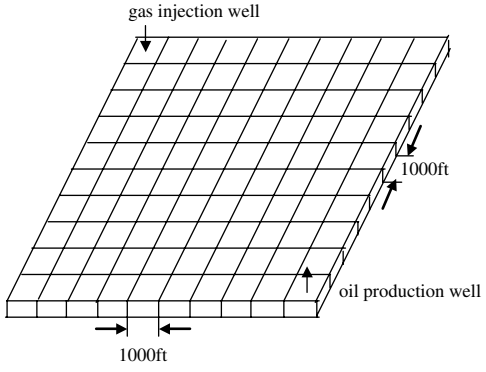

Fig. 4. A grid of rectangular parallelepipeds.

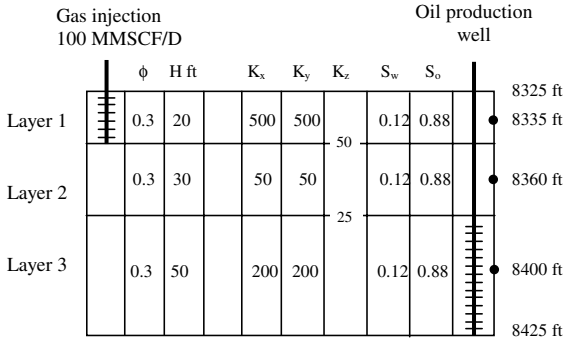

Fig. 5. Diagonal cross-sectional view.

Table 1
Saturated oil PVT function data

Pressure (psia)	FVF (RB/STB)	Viscosity (cp)	Density (lbm/cu ft)	Solution GOR (SCF/STB)
14.7	1.0620	1.0400	46.244	1.0
264.7	1.1500	0.9750	43.544	90.5
514.7	1.2070	0.9100	42.287	180.0
1014.7	1.2950	0.8300	41.004	371.0
2014.7	1.4350	0.6950	38.995	636.0
2514.7	1.5000	0.6410	38.304	775.0
3014.7	1.5650	0.5940	37.781	930.0
4014.7	1.6950	0.5100	37.046	1270.0
5014.7	1.8270	0.4490	36.424	1618.0
9014.7	2.3570	0.2030	36.482	2984.0

Table 2
Saturated water PVT function data

Pressure (psia)	FVF (RB/STB)	Viscosity (cp)	Density (lbm/cu ft)	Gas/water ratio (SCF/STB)
14.7	1.0410	0.3100	62.238	0.0
264.7	1.0403	0.3100	62.283	0.0
514.7	1.0395	0.3100	62.328	0.0
1014.7	1.0380	0.3100	62.418	0.0
2014.7	1.0350	0.3100	62.599	0.0
2514.7	1.0335	0.3100	62.690	0.0
3014.7	1.0320	0.3100	62.781	0.0
4014.7	1.0290	0.3100	62.964	0.0
5014.7	1.0258	0.3100	63.160	0.0
9014.7	1.0130	0.3100	63.959	0.0

Table 3
Gas PVT function data

Pressure (psia)	FVF (RB/STB)	Viscosity (cp)	Density (lbm/cu ft)	Pseudo gas potential (psia/cp)
14.7	0.166666	0.008000	0.0647	0.
264.7	0.012093	0.009800	0.8916	0.777916 E+07
514.7	0.006274	0.011200	1.7185	0.267580 E+08
1014.7	0.003197	0.014000	3.3727	0.875262 E+08
2014.7	0.001614	0.018900	6.6806	0.270709 E+09
2514.7	0.001294	0.020800	8.3326	0.386910 E+09
3014.7	0.001080	0.022800	9.9837	0.516118 E+09
4014.7	0.000811	0.026800	13.2952	0.803963 E+09
5014.7	0.000649	0.030900	16.6139	0.112256 E+10
9014.7	0.000386	0.047000	27.9483	0.251845 E+10

Table 4
Undersaturated oil PVT function data

Pressure (psia)	FVF (RB/STB)	Viscosity (cp)	Density (lbm/cu ft)
4014.7	1.6950	0.5100	37.046
9014.7	1.5790	0.7400	39.768

Table 5
Undersaturated water PVT function data

Pressure (psia)	FVF (RB/STB)	Viscosity (cp)	Density (lbm/cu ft)
4014.7	1.0290	0.3100	62.964
9014.7	1.0130	0.3100	63.959

Table 6
Relative permeability data of the benchmark problem

s_g	k_{rg}	k_{ro}
0.0	0.0	1.0
0.001	0.0	1.0
0.02	0.0	0.997
0.05	0.005	0.980
0.12	0.025	0.700
0.2	0.075	0.350
0.25	0.125	0.200
0.30	0.190	0.090
0.40	0.410	0.021
0.45	0.60	0.010
0.50	0.72	0.001
0.60	0.87	0.0001
0.70	0.94	0.000
0.85	0.98	0.000
1.0	1.0	0.000

There are a gas injection well and an oil production well, whose wellbore radii are 0.25 ft. Their locations are shown in Figs. 4 and 5. They are completely perforated at the first and third zone, respectively. The gas injection rate is 100 MMSCF/D. The maximum and minimum oil production rates of the production well are, respectively, 20,000 and 1000 STB/D, and the minimum flowing bottom hole pressure is 1000 psia. The run of our simulator is terminated at the end of the 10th year.

For the case that the bubble point pressure varies with the gas saturation, we report: (a) the oil production rate vs time and GOR vs time, (b) the pressure vs time, bubble point pressure vs time, and gas saturation vs time at the perforated zone of the production well, and (c) the gas saturation at grid blocks (1,1,1), (1,1,2), (1,1,3), (10,1,1), (10,1,2), (10,1,3), (10,10,1), (10,10,2), and (10,10,3).

The coarseness of grids might affect the production of free gas. To check this, we performed numerical experiments with an increasing number of grids: 447×3, 1548×3, 5850×3, and 22737×3. Fig. 13 shows the comparison results for the gas saturation at the well production grid block. We clearly see that free gas is still generated with grid refinement. This figure also demonstrates convergence of the numerical solution scheme.

To check the accuracy, stability, and convergence of the CVFA methods, we also solve the same problem using the 5-point FD, 9-point FD, and CVFE methods. For the CVFA and CVFE methods, we use hexagonal prisms (hexagons in the x_1x_2-plane and rectangles in the x_3-coordinate direction, see Fig. 2), as base grid blocks to model the structure of a reservoir and reduce grid orientation; since hexagons can reduce grid orientation effects [6], but we are developing 3D grids to simulate multiphase flows in general porous media. In order to have the wells locate at the destination positions, the base grid blocks are adjusted with the technique of corner point correction, as seen in Fig. 6. The total

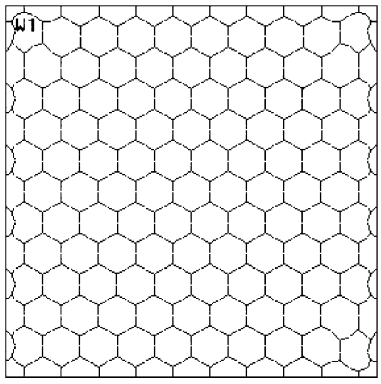

Fig. 6. Cross-section in the x_1x_2-plane of the grid used by the CVFA.

number of grid blocks is 149×3 for these two methods, where 3 is the number of layers. The maximum saturation and maximum pressure changes during the computational processes are set to 0.05 and 500 psi, respectively. Since the permeabilities in the x_1- and x_2-directions are the same in a horizontal plane, the drainage radius of the grid block, in which a well falls, is calculated by

$$r_e = 0.2\sqrt{A},$$

where A indicates the cross-sectional area of this grid block. When the CVFA methods are used, the number R_{ij} for the interpolation points is taken as three; see Eq. (2.4).

Figs. 7–15 give comparative results, where CVFA bilinear and CVFA spline denote the CVFA methods with the bilinear and spline interpolants, 5-p FD and 9-p FD stand for the 5-point and 9-point FD methods, sg11, sg12, and sg13 denote the gas saturation at grid blocks (1,1,1), (1,1,2), and (1,1,3), sg21, sg22, and sg23 represent the gas saturation at grid blocks (10,1,1), (10,1,2), and (10,1,3), and sg31, sg32, and sg33 indicate the gas saturation at grid block (10,10,1), (10,10,2), and

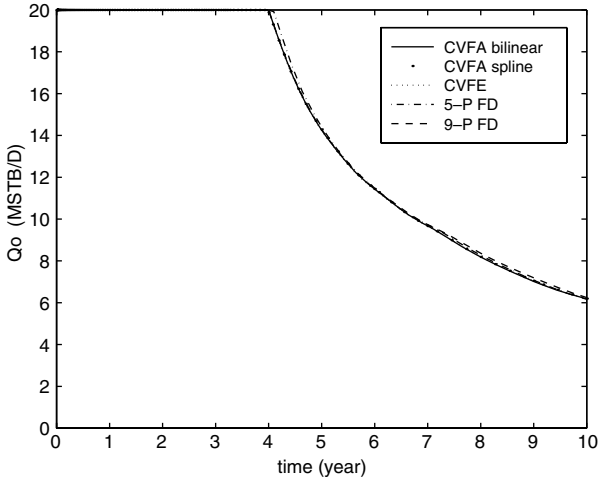

Fig. 7. Oil production rate vs time.

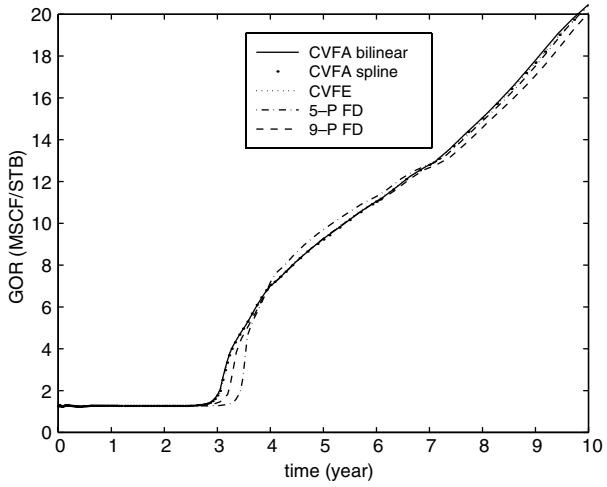

Fig. 8. GOR vs time.

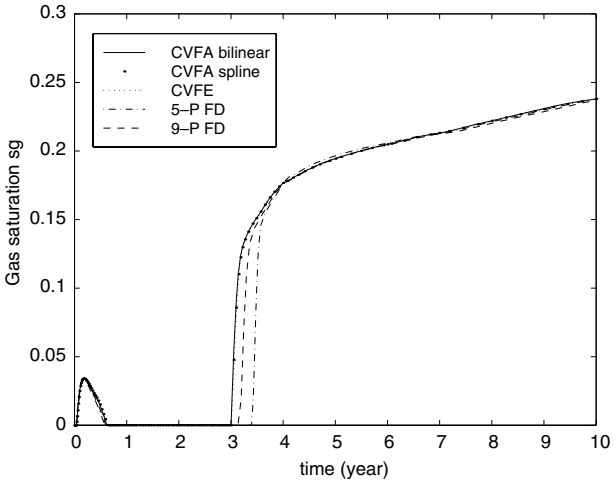

Fig. 11. Gas saturation at the production well block.

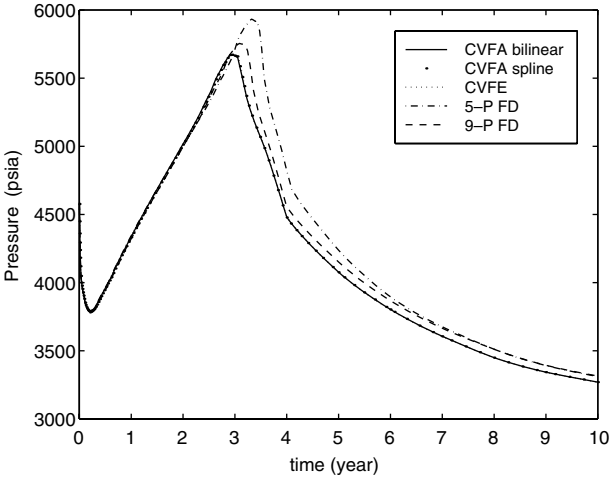

Fig. 9. Pressure at the production well block.

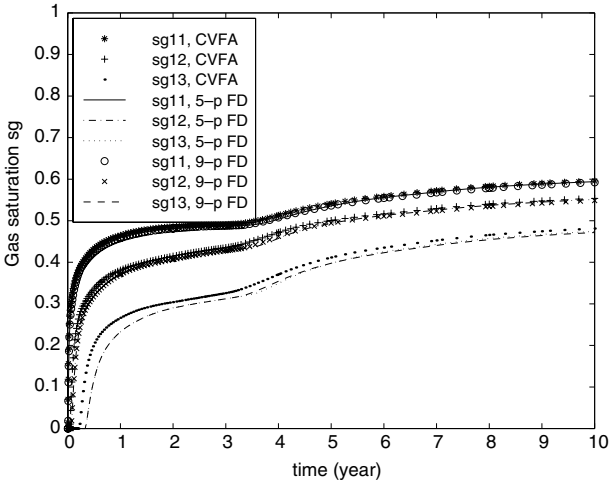

Fig. 12. Gas saturation at blocks (1,1,1), (1,1,2), and (1,1,3).

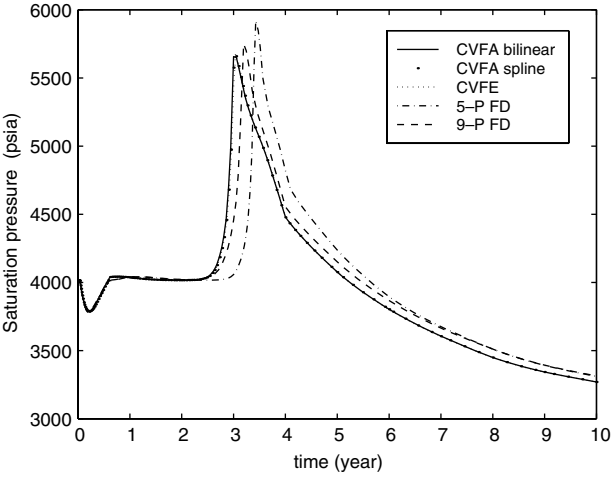

Fig. 10. Bubble point pressure at the production well block.

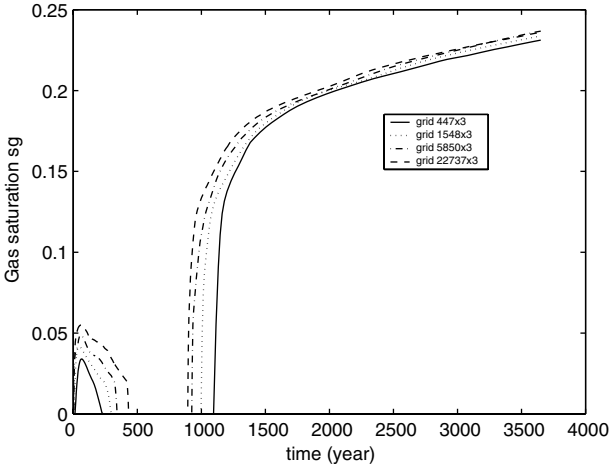

Fig. 13. Gas saturation at the production well block with different grids.

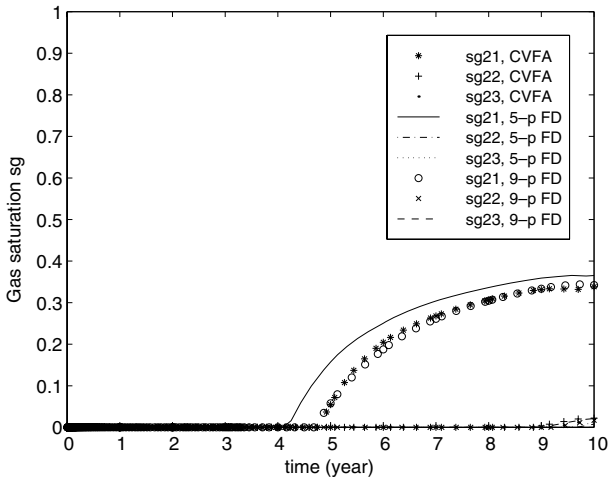

Fig. 14. Gas saturation at blocks (10,1,1), (10,1,2), and (10,1,3).

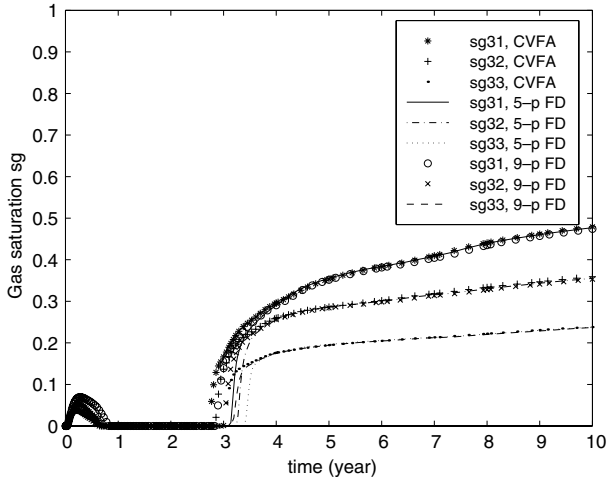

Fig. 15. Gas saturation at blocks (10,10,1), (10,10,2), and (10,10,3).

(10,10,3), respectively. The numerical results obtained from the CVFA and CVFE methods fit perfectly, as seen in Figs. 7–15. The oil production rates obtained by all these discretization methods match very well, as seen in Fig. 7. But there exist some differences between the CVFA and the FD methods for the GOR, reservoir pressure, and bubble point pressure at the production block. The uprising time for the 5-point FD, 9-point FD, and CVFA methods with bilinear interpolation are 3.18, 2.77, and 2.73 years, respectively. The summit time and value of the reservoir pressure at the production block are 2.946 years and 5670.799 psia for the CVFA method with bilinear interpolation, 3.088 years and 5754.693 psia for the 9-point FD method, and 3.321 years and 5933.248 psia for the 5-point FD method. The peak time and value of the bubble point pressure at the production block are 3.000 years and 5657.299 psia for the CVFA method with bilinear interpolation, 3.194 years and 5750.147 psia for the 9-point FD method, and 3.428 years and 5919.499 psia for the 5-point FD method. It is obvious that the results of the CVFA method are closer to those of the 9-point FD method. The plots of the gas saturation vs time also show these observations.

The differences between the results of the 5-point FD method and the results of the other methods indicate that the latter methods are more accurate. It is known that the 9-point FD method has less grid orientation effect than the 5-point FD method. Therefore, the closeness of the results of the CVFA method to those of the 9-point method implies that the CVFA method has less grid orientation effect. This will further be discussed below.

There exists free gas at the production block during the first operation year, which was not reported in [8]. From the plots of the pressure vs time and the bubble point pressure vs time at the production block, we see that the reservoir pressure drops to the bubble point pressure during the early period of the first operation year. It means that the reservoir at the production block enters the saturated state. Therefore, the free gas comes out of the oil phase.

As noted earlier and observed in [6], the CVFA methods can reduce grid orientation effects if hexagonal prisms are used as grid blocks. From Fig. 12, we can see that the injected free gas flows into the production block at about 3.00 years for the CVFA methods, at 3.15 years for the 9-point FD method, and at 3.40 years for the 5-point FD method. However, Fig. 15 shows that the injected free gas enters block (10,1,1) at about 4.70 years for the CVFA method, 4.65 years for the 9-point FD method, and 4.20 years for the 5-point FD method. This phenomenon can be explained from the grid orientation effect. The FD methods have stronger grid orientation effect; i.e., the fluids move more quickly in the direction of coordinate axes than in the diagonal direction of the grid. The production well is in the diagonal direction, while block (10,1,1) is in the coordinate direction from the injection well. Hence the free gas enters block (10,1,1) first and flows into the production block last for the 5-point FD method. The 9-point FD method has less grid orientation effect than the 5-point FD method. Figs. 12–15 indicate that the CVFA method has even less effect than the 9-point FD method.

To check the ability of the CVFA methods to deal with simulation models of large sizes, the simulation model used by the CVFA and CVFE methods is refined in the x_1x_2-plane to a model of 22,737 grid blocks. Note that since the fully implicit solution technique is used, there are three unknown variables at each node for the black oil model. The simulation model used by the FD methods is refined in the x_1x_2-plane to a $87\times87\times3$ model to have a comparative computation between different discretization methods. The linear equation solver used for our numerical simulations is developed based on the ORTHOMIN iterative method with pre-

Table 7
Computational results and costs for refined models from different methods

Method	CVFA bilinear	CVFA spline	CVFE	5-point FD	9-point FD
Number of node	22,737	22,737	22,737	22,707	22,707
Oil recovery (%)	15.48	15.50	15.50	15.41	15.46
Water recovery (%)	87.04	87.64	87.86	88.36	87.36
Oil prod. rate (STB/D)	5922.42	5868.85	5879.43	5855.35	5875.31
Gas prod. rate (MMSCF/D)	128.96	130.40	130.35	129.03	128.90
GOR (MSCF/STB)	21.78	22.22	22.17	22.04	21.94
Time cuts	0	0	0	0	0
Newton iterations	2443	2447	2448	2874	2284
Total CPU time (s)	93235.00	93134.21	92157.23	80390.01	102223.38
Linear solver CPU time (s)	81049.02	80955.10	80842.77	73404.31	94544.57

conditioning of incomplete LU factorization [11]. The error tolerance of the ORTHOMIN iterations for all methods is set to 10^{-4}. Table 7 gives the computational results and costs at 10 years. We can see that the CVFA methods are still stable and convergent for a large model. The computational results of the CVFA methods match with those from the CVFE method and the 9-point FD method very well. The computational cost of the CYFA methods is close to that of the CVFE method, is 0.912 times that of the 9-point FD method, and is 1.16 times that of the 5-point FD method.

Table 7 shows that the computational costs to solve the linear equation systems arising from the CVFA methods are about 87% of the total CPU time. Therefore, reducing the computational costs for linear solvers is the most efficient approach to accelerate a simulation. We are developing other linear solvers such as the GMRES with more sophisticated multilevel preconditioners.

4.2. Three phase coning

The coning problem is caused by the large gradient of a phase potential in the axis direction of a well [2]. In the initial stage of a recovery process of a reservoir, the equal-potential surface has the shape of a semi-sphere with an infinite radius, and the gradient of the potential on the surface is zero everywhere. After a producer is perforated, this gradient will no longer be zero. In the axis direction of the well, it reaches a highest value because of producing. This results in that the shape of the equal-potential surface will change. It gradually changes into a cone, and the top of the cone is toward the perforated zones of the producer. Therefore, the water and/or gas fronts gradually reach at the perforated zones of this producer. Near the wellbore, the saturations and pressure change very rapidly during the formation of water and/or gas coning. This may cause the unstability of a reservoir simulator.

The second SPE CSP [12] was designed to test the stability of reservoir simulators to deal with a coning problem. We use it to test the stability of our new method. Here we briefly review the physical data of this benchmark problem; for more details, see [12]. A cross-sectional view of the reservoir is seen in Fig. 16. The reservoir dimensions, permeabilities, and porosities are presented in Table 8, where k_h and k_v denote the horizontal and vertical permeabilities, respectively. The radial extent of the reservoir is 2050 ft. In the radial direction, 10 blocks are used. Their boundaries are at 2.00, 4.32, 9.33, 20.17, 43.56, 94.11, 203.32, 439.24, 948.92, and 2050 ft, respectively. There are 15 vertical layers. The depth to the top of formation is 9000 ft. The pore, water, oil, undersaturated oil, and oil viscosity compressibilities are 4×10^{-6}, 4×10^{-6}, 3×10^{-6}, and 0 psi^{-1}, respectively. The stock-tank densities for oil and

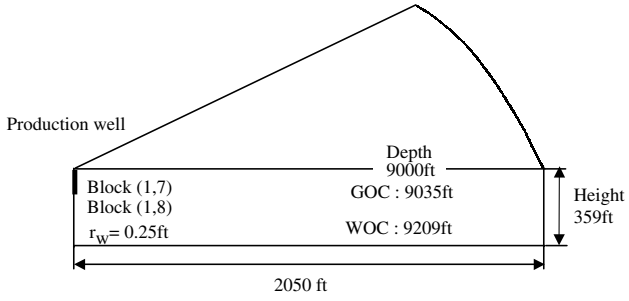

Fig. 16. Cross-sectional view of the reservoir.

Table 8
Reservoir description

Layer	Thickness (ft)	k_h (md)	k_v (day)	Porosity
1	20	35.000	3.500	0.087
2	15	47.500	4.750	0.097
3	26	148.000	14.800	0.111
4	15	202.000	20.200	0.160
5	16	90.000	9.000	0.130
6	14	418.500	41.850	0.170
7	8	775.000	77.500	0.170
8	8	60.000	6.000	0.080
9	18	682.000	68.200	0.140
10	12	472.000	47.200	0.130
11	19	125.000	12.500	0.120
12	18	300.000	30.000	0.105
13	20	137.000	13.750	0.120
14	50	191.000	19.100	0.116
15	100	350.000	35.000	0.157

water are 45.0 and 63.02 lbm/cu ft. The gas density at the standard condition is 0.0702 lbm/cu ft. The depths to the gas/oil contact (GOC), which is the interface between the gas zone and oil zone, and water/oil contact (WOC), which is the interface between water zone and oil zone, are 9035 and 9209 ft, respectively. The reservoir is initially at capillary/gravity equilibrium with a pressure of 3600 psia at the GOC. The capillary pressures at the GOC and WOC are zero. The single well at the center of the radial system is completely perforated at the seventh and eighth layers, has the wellbore radius 0.25 ft, and has a minimum bottom hole pressure of 3000 psia. The saturation function data and PVT property data are presented in Tables 9–11 and the well production schedule is shown in Table 12.

To model the radial flow pattern of this single well, we use a hybrid grid to present the reservoir (see Fig. 17) and apply the CVFA methods to discretize the governing equations. The center blocks are cylinders, and other blocks are obtained by uniformly partitioning in the angular direction. The total number of grid blocks is $(18\times 9+1)\times 15$. The radial sizes of gird blocks are the same as those given in the problem statement. The drainage radius of the center grid blocks, which are cylindrical grid blocks, is

$$r_e = \sqrt{r_c r_1},$$

Table 9
Saturation function data for water/oil

s_w	k_{rw}	k_{row}	P_{cow} (psi)
0.22	0.0	1.0	7.0
0.30	0.07	0.4000	4.0
0.40	0.15	0.1250	3.0
0.50	0.24	0.0649	2.5
0.60	0.33	0.0048	2.0
0.80	0.65	0.0	1.0
0.90	0.83	0.0	0.5
1.00	1.0	0.0	0.0

Table 10
Saturation function data for gas/oil

s_g	k_{rg}	K_{rog}	p_{cgo} (psi)
0.0	0.0	1.0	0.0
0.04	0.0	0.60	0.2
0.10	0.0220	0.33	0.5
0.20	0.1000	0.10	1.0
0.30	0.2400	0.02	1.5
0.40	0.3400	0.0	2.0
0.50	0.4200	0.0	2.5
0.60	0.5000	0.0	3.0
0.70	0.8125	0.0	3.5
0.78	1.0	0.0	3.9

Table 12
Production schedule

Period number	Time period (day)	Oil production rate (STB/D)
1	1–10	1,000
2	10–50	100
3	50–720	1,000
4	720–900	100

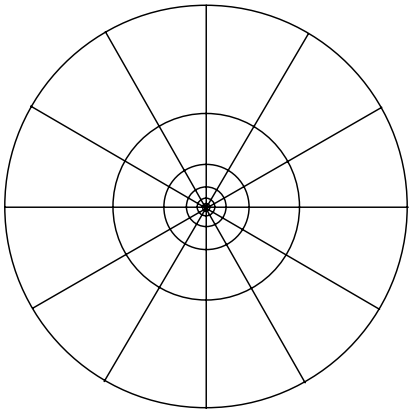

Fig. 17. Cross-sectional view of the grid system.

Table 11
PVT property data

P (psia)	B_o (RB/STB)	μ_o (cp)	R_{so} (SCF/STB)	B_w (RB/STB)	μ_w (cp)	B_g (RB/STB)	μ_g (cp)
400	1.0120	1.17	165	1.01303	0.96	5.90	0.0130
800	1.0255	1.14	335	1.01182	0.96	2.95	0.0135
1200	1.0380	1.11	500	1.01061	0.96	1.96	0.0140
1600	1.0150	1.08	665	1.00940	0.96	1.47	0.0145
2000	1.0630	1.06	828	1.00820	0.96	1.18	0.0150
2400	1.0750	1.03	985	1.00700	0.96	0.98	0.0155
2800	1.0870	1.00	1130	1.00580	0.96	0.84	0.0160
3200	1.0985	0.98	1270	1.00460	0.96	0.74	0.0165
3600	1.1100	0.95	1390	1.00341	0.96	0.65	0.0170
4000	1.1200	0.94	1500	1.00222	0.96	0.59	0.0175
4400	1.1300	0.92	1600	1.00103	0.96	0.54	0.0180
4800	1.1400	0.91	1676	0.99985	0.96	0.49	0.0185
5200	1.1480	0.90	1750	0.99866	0.96	0.45	0.0190
5600	1.1550	0.89	1810	0.99749	0.96	0.42	0.0195

where r_1 indicates the radius of the center block and r_c is the wellbore radius. For the center grid blocks, the total number of interpolation points is 19. For other grid blocks, we take one as the value of the interpolation parameter R_{ij}; see Section 2. To choose appropriate time steps, the maximum saturation change is set to 0.05.

We just compare the CVFA with FD methods for this three-phase coning problem since the CVFE uses grids based on triangles or tetrahedra and cannot accurately model the cylindrical boundary of this problem. The FD method in a (r,z)-coordinate system is adopted to carry out the computations. The total number of grid blocks is 10×15.

Fig. 18 shows the plot of initial saturations vs depth. The gas saturation drops to zero if the depth is greater than 9035 ft, which is consistent with the given positions of the given GOC and WOC. Also, the initial saturations satisfy the constraint (3.6). Table 13 shows the initial fluids in place. Figs. 19–23 give the plots of the oil production rate vs time, water cut vs time, GOR vs time, bottom hole pressure vs time, and pressure drawdown (p(1,7)-bhp) vs time for the CVFA and FD methods, where bhp stands for the bottom hole pressure and p(1,7) is the reservoir pressure at the first radial grid block and the seventh layer. There are slight differences between the two methods for the bottom hole pressure and pressure drawdown (p(1,7)-bhp). Also, small differences occur between them for the oil production rate, water cut, and GOR.

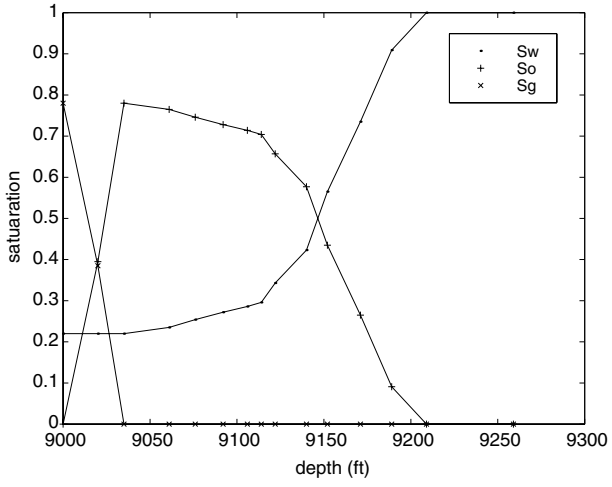

Fig. 18. Initial saturation distribution.

Table 13
Initial fluids in place and time on decline

Method	Oil (10^6 STB)	Water (10^6 STB)	Gas (10^6 STB)	Time on decline (day)
FD	28. 87	73.98	47.13	230
CVFA	28.89	73.96	47.08	220

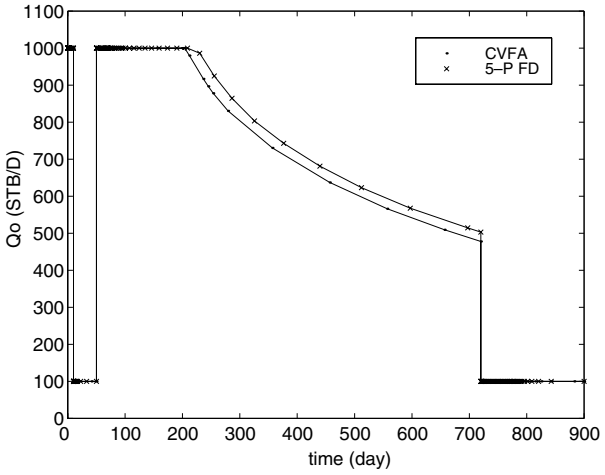

Fig. 19. Oil production rate vs time.

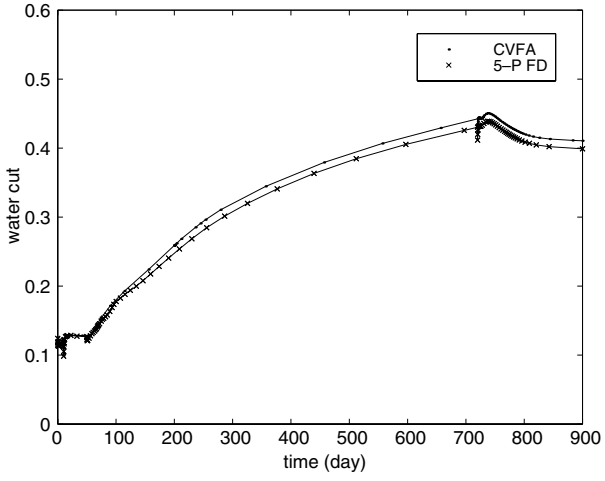

Fig. 20. Water cut vs time.

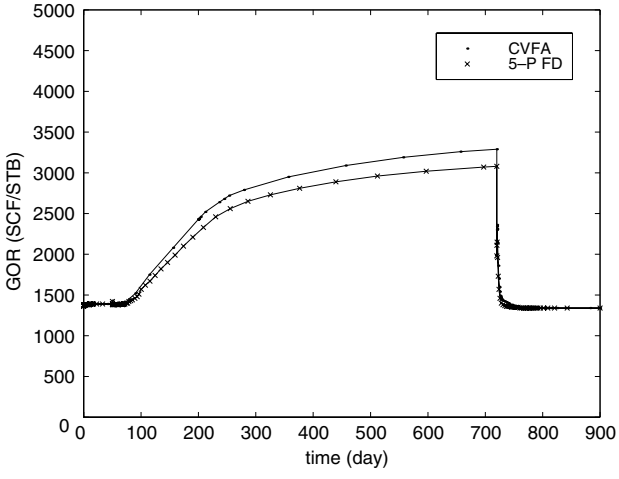

Fig. 21. GOR vs time.

To check the stability of the CVFA methods to deal with stronger coning, we design another three cases A,

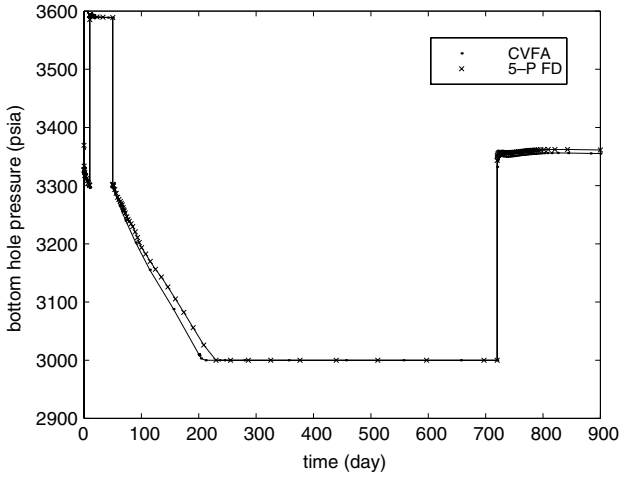

Fig. 22. Bottom hole pressure vs time.

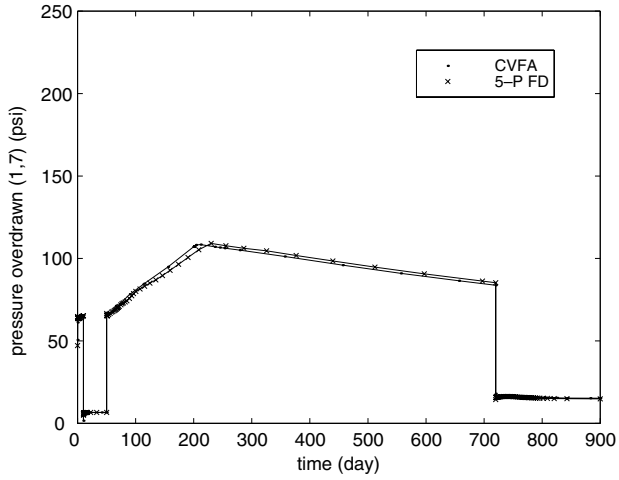

Fig. 23. Pressure drawdown (1,7) vs time.

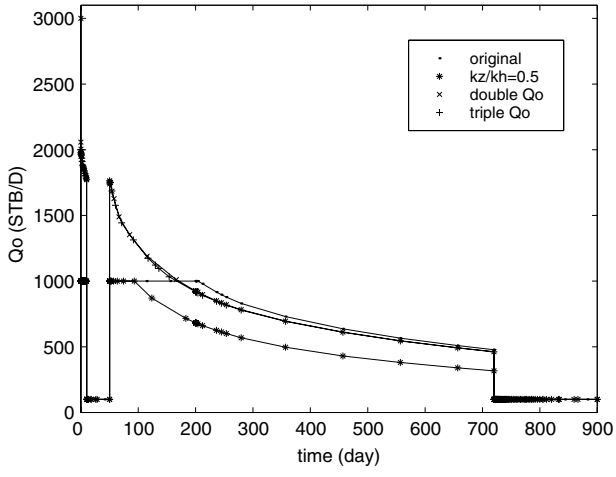

Fig. 24. Oil production rate for different parameters.

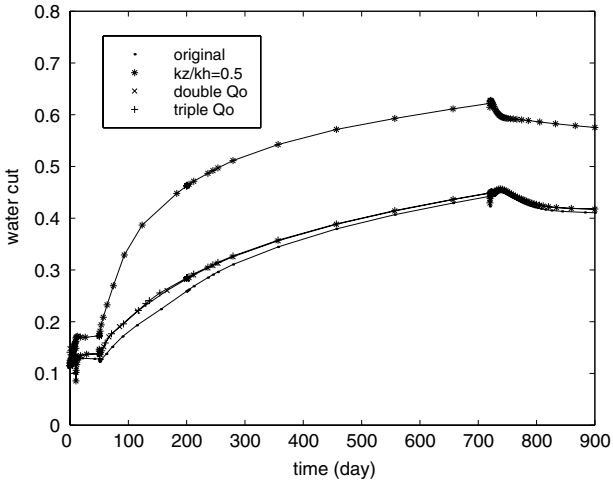

Fig. 25. Water cut for different parameters.

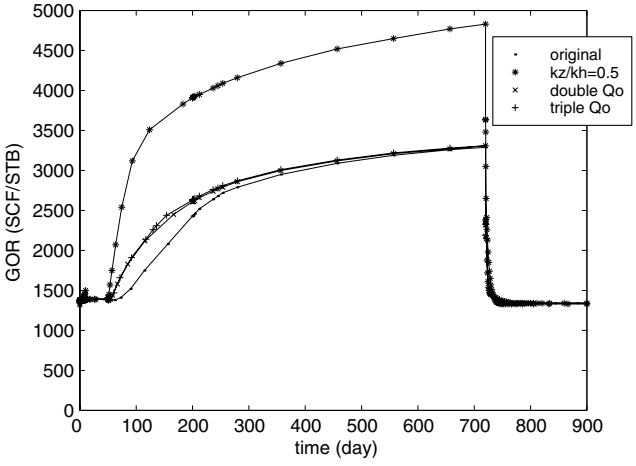

Fig. 26. GOR for different parameters.

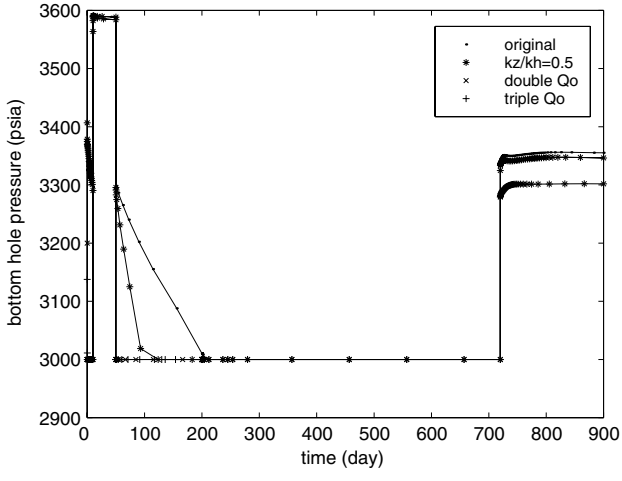

Fig. 27. Bottom hole pressure for different parameters.

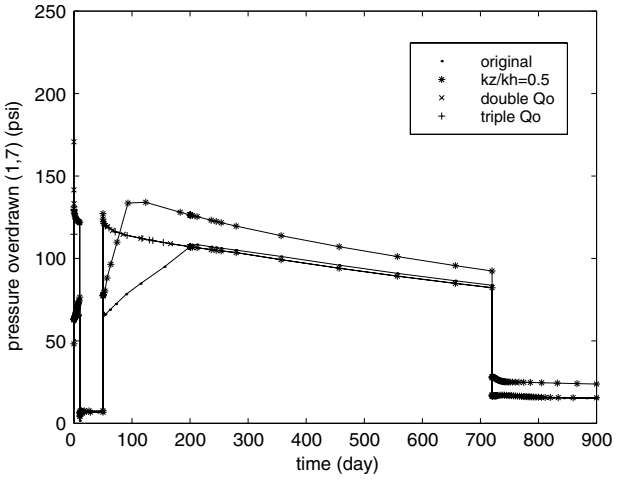

Fig. 28. Pressure overdrawn (1,7) for different parameters.

B, and C by changing the ratio of the vertical permeability to the horizontal permeability k_v/k_h from 0.1 to 0.5 for case A, changing $Q_{0,\max}$ (the maximum oil production rate) from 1000 to 2000 STB/D for case B, and changing $Q_{0,\max}$ from 1000 to 3000 STB/D for case C based on the original data. Figs. 24–28 are the oil production rate vs time, water cut vs time, GOR vs time, bottom hole pressure vs time, and pressure drawdown at block (1,7) for these cases. We can see that water and gas coning becomes more serious, if k_v/k_h changes to 0.5; the transients become significant if the maximum oil production rate is doubled or tripled. But no oscillations occur.

5. Conclusions

In this paper we have extended the CVFA methods to three-dimensional space and also briefly analyzed their relationships to the FD, PEBI, and CVFE methods. We have applied them to the discretization of the governing equations of the black oil model and checked the stability and convergence of the CVFA methods to deal with the bubble point and coning problems, which are the well-known difficult problems in reservoir simulation, by using the benchmark problems of the first and second SPE CSPs.

The numerical experiment results have shown that these new methods are conver gent, stable, and accurate in dealing with the bubble point problem and three-phase coning of the black oil model, with the fully implicit solution method. The simulation experiments demonstrate that these methods reduce grid orientation effects with proper grids. Compared with the FD and CVFE methods, they can more easily use arbitrarily shaped grid blocks, which are needed to represent accurately and efficiently flow patterns and complicated geometrical features of a reservoir. Although the CVFA methods appear more complicated, our numerical experiments show that their computational cost increases by less than 0.2 times that of the 5-point FD method, is less than that of the 9-point FD method, and is close to that of the CVFE method. Our development experience of a reservoir simulator shows that 70–80% existing subroutines can be reused by the CVFA methods, since their discrete form of the governing equations is very similar to those by the FD and CVFE methods. Therefore, it is easy to integrate them with the existing simulator software developed using the FD and CVFE methods.

Appendix A. Linearization of the governing equations and well control equations

In this appendix we carry out the linearization of the governing equations of the black oil model using Newton–Raphson's procedure. Again, the unknown variables are different under the different states of a reservoir, so we discuss them separately.

A.1. Undersaturated state

Under the undersaturated state, the unknowns are $p = p_0$, s_w, and p_b. After substitution of Eq. (3.4) into Eqs. (3.1)–(3.3), the integral forms of the resulting equations on each control volume V_i, $i = 1, 2, \ldots, N$, can be discretized by the backward Euler difference method in time and linearized by the Newton–Raphson procedure as follows:

$$
\begin{aligned}
&\int_{\partial V_i} \left\{ \frac{KK_{rw}}{\mu_w}\frac{\rho_{WS}}{B_w} + KK_{rw}\frac{\partial}{\partial p}\left(\frac{\rho_{WS}}{\mu B_w}\right)\delta p \right.\\
&\left. + \frac{K\rho_{WS}}{\mu_w B_w}\frac{\partial K_{rw}}{\partial s_w}\delta s_w \right\}_l^{(n+1)} (\nabla \Phi_w)^{(n+1)} \cdot \mathbf{n}\,\mathrm{d}A\\
&+ \int_{\partial V_i} \left[\frac{KK_{rw}}{\mu_w}\frac{\rho_{WS}}{B_w}\nabla(\delta p)\right]_l^{(n+1)} \cdot \mathbf{n}\,\mathrm{d}A\\
&- \int_{\partial V_i} \left[\frac{KK_{rw}}{\mu_w}\frac{\rho_{WS}}{B_w}\nabla\left(\frac{\partial p_{cow}}{\partial s_w}\delta s_w\right)\right]_l^{(n+1)} \cdot \mathbf{n}\,\mathrm{d}A\\
&+ \sum_{k=1}^{N_w}\sum_{m=1}^{M_{w,k}} \int_{V_i} \left\{ q_{w,k,m} + \frac{\mu_w B_w}{\rho_{WS}} q_{w,k,m}\frac{\partial}{\partial p}\left(\frac{\partial_{WS}}{\mu_w B_w}\right)\delta p \right.\\
&\left. + \frac{q_{w,k,m}}{K_{rw}}\frac{\partial K_{rw}}{\partial s_w}\delta s_w + \mathrm{WI}_{k,m}\frac{K_{rw}\rho_{WS}}{\mu_w B_w}(\delta p_{bh,k} - \delta p) \right\}_l^{(n+1)}\\
&\times \delta_{k,m}\,\mathrm{d}\mathbf{x} = \frac{V_i}{\Delta t_n}\left\{ \left(\phi\frac{\rho_{WS}}{B_w}s_w\right)_l^{(n+1)} - \left(\phi\frac{\phi_{WS}}{B_w}s_w\right)^{(n)} \right.\\
&+ \left(\phi\frac{\rho_{WS}}{B_w}\right)_l^{(n+1)} (\delta s_w)_l^{(n+1)} + \left[c_r\phi_a\frac{\rho_{WS}}{B_w}s_w \right.\\
&\left.\left. + \phi s_w\frac{\partial}{\partial p}\left(\frac{\rho_{WS}}{B_w}\right)\right]_l^{(n+1)} (\delta p)_l^{(n+1)} \right\}_{\mathbf{x}=\mathbf{x}_i},
\end{aligned}
$$

$$\int_{\partial V_i}\left\{\frac{KK_{ro}}{\mu_o}\frac{\rho_{OS}}{B_o}+KK_{ro}\frac{\partial}{\partial p}\left(\frac{\rho_{OS}}{\mu_oB_o}\right)\delta p+\frac{K\rho_{OS}}{\mu_oB_o}\frac{\partial K_{ro}}{\partial s_w}\delta s_w+KK_{ro}\frac{\partial}{\partial p_b}\left(\frac{\rho_{OS}}{\mu_oB_o}\right)\delta p_b\right\}_l^{(n+1)}\times(\nabla\Phi_o)_l^{n+1}\cdot\mathbf{n}\,dA\int_{\partial V_i}\left[\frac{KK_{ro}}{\mu_o}\frac{\rho_{OS}}{B_o}\nabla(\delta p)\right]_l^{(n+1)}\cdot\mathbf{n}\,dA+\sum_{k=1}^{N_w}\sum_{m=1}^{M_{w,k}}\int_{V_i}\left\{q_{o,k,m}-WI_{k,m}\frac{K_{ro}\rho_{OS}}{\mu_oB_o}(\delta p-\delta p_{bh,k})+\frac{\mu_oB_o}{\rho_{OS}}q_{o,k,m}\frac{\partial}{\partial p}\left(\frac{\rho_{OS}}{\mu_oB_o}\right)\delta p+\frac{q_{o,k,m}}{K_{ro}}\frac{\partial K_{ro}}{\partial s_w}\delta s_w+\frac{\mu_oB_o}{\rho_{OS}}q_{o,k,m}\frac{\partial}{\partial p_b}\left(\frac{\rho_{OS}}{\mu_oB_o}\right)\delta p_b\right\}_l^{(n+1)}\delta_{k,m}\,d\mathbf{x}$$
$$=\frac{V_i}{\Delta t_n}\left\{\left(\phi\frac{\rho_{OS}}{B_o}s_o\right)_l^{(n+1)}-\left(\phi\frac{\rho_{OS}}{B_o}s_o\right)^{(n)}+\left[\phi s_o\frac{\partial}{\partial p_b}\left(\frac{\rho_{OS}}{B_o}\right)\right]_l^{(n+1)}(\delta p_b)_l^{(n+1)}+\left[c_r\phi_a\frac{\rho_{OS}}{B_o}s_o+\phi s_o\frac{\partial}{\partial p}\left(\frac{\rho_{OS}}{B_o}\right)\right]_l^{(n+1)}\times(\delta p)_l^{(n+1)}.-\left(\phi\frac{\rho_{OS}}{B_o}\right)_l^{(n+1)}(\delta s_w)_l^{(n+1)}\right\}_{\mathbf{x}=\mathbf{x}_i},$$

and

$$\int_{\partial V_i}\left\{\frac{KK_{ro}}{\mu_o}\frac{R_{so}\rho_{GS}}{B_o}+KK_{ro}\frac{\partial}{\partial p}\left(\frac{R_{so}\rho_{GS}}{\mu_oB_o}\right)\delta p+\frac{KR_{so}\rho_{GS}}{\mu_oB_o}\frac{\partial K_{ro}}{\partial s_w}\delta s_w+KK_{ro}\frac{\partial}{\partial p_b}\left(\frac{R_{so}\rho_{GS}}{\mu_oB_o}\right)\delta p_b\right\}_l^{(n+1)}\times(\nabla\Phi_o)_l^{(n=1)}\cdot\mathbf{n}\,dA\int_{\partial V_i}\left[\frac{KK_{ro}}{\mu_o}\frac{R_{so}\rho_{GS}}{B_o}\nabla(\delta p)\right]_l^{(n+1)}\cdot\mathbf{n}\,dA\sum_{k=1}^{N_w}\sum_{m=1}^{M_{w,k}}\int_{V_i}\left\{q_{o,k,m}^G+\frac{\mu_oB_o}{R_{so}\rho_{GS}}q_{o,k,m}^G\times\frac{\partial}{\partial p}\left(\frac{R_{so}\rho_{GS}}{\mu_oB_o}\right)\delta p+\frac{q_{o,k,m}^G}{K_{ro}}\frac{\partial K_{ro}}{\partial s_w}\delta s_w+\frac{\mu_oB_o}{R_{so}\rho_{GS}}q_{o,k,m}^G\frac{\partial}{\partial p_b}\left(\frac{R_{so}\rho_{GS}}{\mu_oB_o}\right)\delta p_b+WI_{k,m}\frac{K_{ro}R_{so}\rho_{GS}}{\mu_oB_o}(\delta p_{bh,k}-\delta p)\right\}\delta_{k,m}\,d\mathbf{x}$$
$$=\frac{V_i}{\Delta t_n}\left\{\left(\phi\frac{R_{so}\rho_{GS}}{B_o}s_o\right)_l^{(n+1)}-\left(\phi\frac{R_{so}\rho_{GS}}{B_o}s_o\right)^{(n)}+\left[c_r\phi_a\frac{R_{so}\rho_{GS}}{B_o}s_o+\phi s_o\frac{\partial}{\partial p}\left(\frac{R_{so}\rho_{GS}}{B_o}\right)\right]_l^{(n+1)}\times(\delta p)_l^{(n+1)}-\left(\phi\frac{R_{so}\rho_{GS}}{B_o}s_o\right)_l^{(n+1)}(\delta s_w)_l^{(n+1)}+\left[\phi s_o\frac{\partial}{\partial p_b}\left(\frac{R_{so}\rho_{GS}}{B_o}\right)\right]_l^{(n+1)}(\delta p_b)_l^{(n+1)}\right\}_{\mathbf{x}=\mathbf{x}_i},$$

where n indicates the nth time step and l represents the lth iteration of the Newton–Raphson procedure.

Under this state, the well controls are implicitly treated as follows. For a bottom hole pressure control of a kth well, the bottom pressure is constant:

$$\delta p_{bh,k}=0.$$

For the water injection rate control of a kth well, by (3.8), the well constraint can be treated as

$$\sum_{m=1}^{M_{w,k}}\int_{V_{k,m}}\left\{WI_{k,m}\frac{K_{rw\max}\rho_{WS}}{\mu_wB_w}(\delta p_{bh,k}-\delta p)+q_{wk,m}\left[1+\frac{\mu_wB_w}{\rho_{WS}}\frac{\partial}{\partial p}\left(\frac{\rho_{WS}}{\mu_wB_w}\right)\delta p+\frac{1}{K_{rw}}\frac{\partial K_{rw}}{\partial s_w}\delta s_w\right]\right\}_l^{(n+1)}\delta_{k,m}\,d\mathbf{x}=Q_{W,k}.$$

Similarly, for the oil production rate control of a kth well, the well constraint has the form

$$\sum_{m=1}^{M_{w,k}}\int_{V_{k,m}}\left\{WI_{k,m}\frac{K_{ro}\rho_{OS}}{\mu_oB_o}(\delta p_{bh,k}-\delta p)+q_{ok,m}\left[1+\frac{\mu_oB_o}{\rho_{OS}}\frac{\partial}{\partial p}\left(\frac{\rho_{OS}}{\mu_oB_o}\right)\delta p+\frac{1}{K_{ro}}\frac{\partial K_{ro}}{\partial s_w}\delta s_w+\frac{\mu_oB_o}{\rho_{OS}}\frac{\partial}{\partial p_b}\left(\frac{\rho_{OS}}{\mu_oB_o}\right)\delta p_b\right]\right\}_l^{(n+1)}\delta_{k,m}\,d\mathbf{x}=Q_{O,k},$$

and for the liquid flow rate control of production of a kth well,

$$\sum_{m=1}^{M_{w,k}}\int_{V_{k,m}}\left\{WI_{k,m}\frac{K_{rw}\rho_{WS}}{\mu_wB_w}(\delta p_{bh,k}-\delta p)+q_{wk,m}\left[1+\frac{\mu_wB_w}{\rho_{WS}}\frac{\partial}{\partial p}\left(\frac{\rho_{WS}}{\mu_wB_w}\right)\delta p+\frac{1}{K_{rw}}\frac{\partial K_{rw}}{\partial s_w}\delta s_w\right]+WI_{k,m}\frac{K_{ro}\rho_{OS}}{\mu_oB_o}(\delta p_{bh,k}-\delta p)+q_{ok,m}\left[1+\frac{\mu_oB_o}{\rho_{OS}}\frac{\partial}{\partial p}\left(\frac{\rho_{OS}}{\mu_oB_o}\right)\delta p+\frac{1}{K_{ro}}\frac{\partial K_{ro}}{\partial s_w}\delta s_w+\frac{\mu_oB_o}{\rho_{OS}}\frac{\partial}{\partial p_b}\left(\frac{\rho_{OS}}{\mu_oB_o}\right)\delta p_b\right]\right\}_l^{(n+1)}\delta_{k,m}\,d\mathbf{x}=Q_{L,k}.$$

A.2. Saturated state

Under the saturated state, the unknowns are $p=p_0$, s_w, and s_0. In a similar manner as in A.1, the integral forms of the governing equations are linearized as follows:

$$\int_{\partial V_i}\left\{\frac{KK_{rw}}{\mu_w}\frac{\rho_{WS}}{B_w}+KK_{rw}\frac{\partial}{\partial p}\left(\frac{\rho_{WS}}{\mu_w B_w}\right)\delta p+\frac{K\rho_{WS}}{\mu_w B_w}\frac{\partial K_{rw}}{\partial s_w}\delta s_w\right\}_l^{(n+1)}(\nabla\Phi_w)_l^{(n+1)}\cdot\mathbf{n}\,dA+\int_{\partial V_i}\left[\frac{KK_{rw}}{\mu_w}\frac{\rho_{WS}}{B_w}\Delta(\delta p)\right]_l^{(n+1)}\cdot\mathbf{n}\,dA-\int_{\partial V_i}\left[\frac{KK_{rw}}{\mu_w}\frac{\rho_{WS}}{B_w}\nabla\left(\frac{\partial p_{cow}}{\partial s_w}\delta s_w\right)\right]_l^{(n+1)}\cdot\mathbf{n}\,dA+\sum_{k=1}^{N_w}\sum_{m=1}^{M_{w,k}}\int_{V_i}\left\{q_{w,k,m}+\frac{\mu_w B_w}{\rho_{WS}}q_{w,k,m}\frac{\partial}{\partial p}\left(\frac{\rho_{WS}}{\mu_w B_w}\right)\delta p+\frac{q_{w,k,m}}{K_{rw}}\frac{\partial K_{rw}}{\partial s_w}\delta s_w+WI_{k,m}\frac{K_{rw}\rho_{WS}}{\mu_w B_w}(\delta p_{bh,k}-\delta p)\right\}_l^{(n+1)}\delta_{k,m}\,d\mathbf{x}$$

$$=\frac{V_i}{\Delta t_n}\left\{\left(\phi\frac{\rho_{WS}}{B_w}s_w\right)_l^{(n+1)}-\left(\phi\frac{\rho_{WS}}{B_w}s_w\right)^{(n)}+\left(\phi\frac{\rho_{WS}}{B_w}\right)_l^{(n+1)}(\delta s_w)_l^{(n+1)}+\left[c_r\phi_a\frac{\rho_{WS}}{B_w}s_w+\phi s_w\frac{\partial}{\partial p}\left(\frac{\rho_{WS}}{B_w}\right)\right]_l^{(n+1)}(\delta p)_l^{(n+1)}\right\}_{\mathbf{x}=\mathbf{x}_i},$$

$$\int_{\partial V_i}\left\{\frac{KK_{ro}}{\mu_o}\frac{\rho_{OS}}{B_o}+KK_{ro}\frac{\partial}{\partial p}\left(\frac{\rho_{OS}}{\mu_o B_o}\right)\delta p-\frac{K\rho_{OS}}{\mu_o B_o}\frac{\partial K_{ro}}{\partial s_g}\delta s_o+\frac{K\rho_{OS}}{\mu_o B_o}\left(\frac{\partial K_{ro}}{\partial s_w}-\frac{\partial K_{ro}}{\partial s_g}\right)\delta s_w\right\}_l^{(n+1)}\times(\nabla\Phi_o)_l^{(n+1)}\cdot\mathbf{n}\,dA+\int_{\partial V_i}\left[\frac{KK_{ro}}{\mu_o}\frac{\rho_{OS}}{B_o}\nabla(\delta p)\right]_l^{(n+1)}\cdot\mathbf{n}\,dA+\sum_{k=1}^{N_w}\sum_{m=1}^{M_{w,k}}\int_{V_i}\left\{q_{o,k,m}+\frac{\mu_o B_o}{\rho_{OS}}q_{o,k,m}\frac{\partial}{\partial p}\left(\frac{\rho_{OS}}{\mu_o B_o}\right)\delta p-\frac{q_{o,k,m}}{K_{ro}}\frac{\partial K_{ro}}{\partial s_g}\delta s_o+\frac{q_{o,k,m}}{K_{ro}}\left(\frac{\partial K_{ro}}{\partial s_w}-\frac{\partial K_{ro}}{\partial s_g}\right)\delta s_w+WI_{k,m}\frac{K_{ro}\rho_{OS}}{\mu_o B_o}(\delta p_{bh,k}-\delta p)\right\}_l^{(n+1)}\delta_{k,m}\,d\mathbf{x}$$

$$=\frac{V_i}{\Delta t_n}\left\{\left(\phi\frac{\rho_{OS}}{B_o}s_o\right)_l^{(n+1)}-\left(\phi\frac{\rho_{OS}}{B_o}s_o\right)^{(n)}+\left(\phi\frac{\rho_{OS}}{B_o}\right)_l^{(n+1)}\times(\delta s_o)_l^{(n+1)}+\left[c_r\phi_a\frac{\rho_{OS}}{B_o}s_o+\phi s_o\frac{\partial}{\partial p}\left(\frac{\rho_{OS}}{B_o}\right)\right]_l^{(n+1)}(\delta p)_l^{(n+1)}\right\}_{\mathbf{x}=\mathbf{x}_i}$$

and

$$\int_{\partial V_i}\left\{\frac{KK_{rg}}{\mu_g}\frac{\rho_{GS}}{B_g}+KK_{rg}\frac{\partial}{\partial p}\left(\frac{\rho_{GS}}{\mu_g B_g}\right)\delta p-\frac{K\rho_{GS}}{\mu_g B_g}\frac{\partial K_{rg}}{\partial s_g}\delta s_w-\frac{K\rho_{GS}}{\mu_g B_g}\frac{\partial K_{rg}}{\partial s_g}\delta s_o\right\}_l^{(n+1)}(\nabla\Phi_g)_l^{(n+1)}\cdot\mathbf{n}\,dA+\int_{\partial V_i}\left[\frac{KK_{rg}}{\mu_g}\frac{\rho_{GS}}{B_g}\nabla(\delta p)\right]_l^{(n+1)}\cdot\mathbf{n}\,dA-\int_{\partial V_i}\left[\frac{KK_{rg}}{\mu_g}\frac{\rho_{GS}}{B_g}\nabla\left(\frac{\partial p_{cgo}}{\partial s_g}\delta s_w+\frac{\partial p_{cgo}}{\partial s_g}\delta s_o\right)\right]_l^{(n+1)}\cdot\mathbf{n}\,dA+\int_{\partial V_i}\left\{\frac{KK_{ro}}{\mu_o}\frac{R_{so}\rho_{GS}}{B_o}+KK_{ro}\frac{\partial}{\partial p}\left(\frac{R_{so}\rho_{GS}}{\mu_o B_o}\right)\delta p-\frac{KR_{so}\rho_{GS}}{\mu_o B_o}\frac{\partial K_{ro}}{\partial s_g}\delta s_o+\frac{KR_{so}\rho_{GS}}{\mu_o B_o}\left(\frac{\partial K_{ro}}{\partial s_w}-\frac{\partial K_{ro}}{\partial s_g}\right)\delta s_w\right\}_l^{(n+1)}\times(\nabla\Phi_o)_l^{(n+1)}\cdot\mathbf{n}\,dA+\int_{\partial V_i}\left[\frac{KK_{ro}}{\mu_o}\frac{R_{so\rho_{GS}}}{B_o}\nabla(\delta p)\right]_l^{(n+1)}\cdot\mathbf{n}\,dA+\sum_{k=1}^{N_w}\sum_{m=1}^{M_{w,k}}\int_{V_i}\left\{q^G_{g,k,m}+WI_{k,m}\frac{K_{rg}\rho_{GS}}{\mu_g B_g}(\delta p_{bh,k}-\delta p)+\frac{\mu_g B_g}{\rho_{GS}}q^G_{g,k,m}\frac{\partial}{\partial p}\left(\frac{\rho_{GS}}{\mu_g B_g}\right)\delta p-\frac{q^G_{g,k,m}}{K_{rg}}\frac{\partial K_{rg}}{\partial s_g}(\delta s_w+\delta s_o)\right\}_l^{(n+1)}\times\delta_{k,m}\,d\mathbf{x}+\sum_{k=1}^{N_w}\sum_{m=1}^{M_{w,k}}\int_{V_i}\left\{q^G_{o,k,m}+WI_{k,m}\frac{K_{ro}R_{so}\rho_{GS}}{\mu_o B_o}\times(\delta p_{bh,k}-\delta p)-\frac{q^G_{o,k,m}}{K_{ro}}\frac{\partial K_{ro}}{\partial s_g}\delta s_o+\frac{\mu_o B_o}{R_{so}\rho_{GS}}q^G_{o,k,m}\times\frac{\partial}{\partial p}\left(\frac{R_{so}\rho_{GS}}{\mu_o B_o}\right)\delta p+\frac{q^G_{o,k,m}}{K_{ro}}\left(\frac{\partial K_{ro}}{\partial s_w}-\frac{\partial K_{ro}}{\partial s_g}\right)\delta s_w\right\}_l^{(n+1)}\times\delta_{k,m}\,d\mathbf{x}=\frac{V_i}{\Delta t_n}\left\{\left(\phi\frac{\rho_{GS}}{B_g}s_g\right)_l^{(n+1)}-\left(\phi\frac{\rho_{GS}}{B_g}s_g\right)^{(n)}-\left(\phi\frac{\rho_{GS}}{B_g}\right)_l^{(n+1)}(\delta s_w)_l^{(n+1)}+\left[c_r\phi_a\frac{\rho_{GS}}{B_g}s_g+\phi s_g\frac{\partial}{\partial p}\left(\frac{\rho_{GS}}{B_g}\right)\right]_l^{(n+1)}(\delta p)_l^{(n+1)}-\left(\phi\frac{\rho_{GS}}{B_g}\right)_l^{(n+1)}(\delta s_o)_l^{(n+1)}\right\}_{\mathbf{x}=\mathbf{x}_i}+\frac{V_i}{\Delta t_n}\left\{\left(\phi\frac{R_{so}\rho_{GS}}{B_o}s_o\right)_l^{(n+1)}-\left(\phi\frac{R_{so}\rho_{GS}}{B_o}s_o\right)^{(n)}+\left[c_r\phi_a\frac{R_{so}\rho_{GS}}{B_o}s_o+\phi s_o\frac{\partial}{\partial p}\left(\frac{R_{so}\rho_{GS}}{B_o}\right)\right]_l^{(n+1)}(\delta p)_l^{(n+1)}+\left(\phi\frac{R_{so}\rho_{GS}}{B_o}\right)_l^{(n+1)}\times((\delta s_o)_l^{(n+1)})_l^{(n+1)}\right\}_{\mathbf{x}=\mathbf{x}_i}.$$

Under the saturated state, the bottom hole pressure and water injection rate controls have the same form as those under the undersaturated state. The gas injection and production rate controls are, respectively, treated as

$$\sum_{m=1}^{M_{w,k}} \int_{V_{k,m}} \left\{ \mathrm{WI}_{k,m} \frac{K_{rg\max}\rho_{GS}}{\mu_g B_g} (\delta p_{bh,k} - \delta p) + q^G_{g,k,m} \left[1 + \frac{\mu_g B_g}{\rho_{GS}} \frac{\partial}{\partial p} \left(\frac{\rho_{GS}}{\mu_g B_g} \right) \delta p - \frac{1}{K_{rg}} \frac{\partial K_{rg}}{\partial s_g} (\delta s_w + \delta s_o) \right] \right\}_l^{(n+1)} \delta_{k,m} \, d\mathbf{x} = Q_{G,K}.$$

and

$$\sum_{m=1}^{M_{w,k}} \int_{V_{k,m}} \left\{ \mathrm{WI}_{k,m} \left[\frac{K_{rg}\rho_{GS}}{\mu_g B_g} + \frac{K_{ro}R_{so}\rho_{GS}}{\mu_o B_o} \right] (\delta p_{bh,k} - \delta p) + q^G_{g,k,m} \left[1 + \frac{\mu_g B_g}{\rho_{GS}} \frac{\partial}{\partial p} \left(\frac{\rho_{GS}}{\mu_g B_g} \right) \delta p - \frac{1}{K_{rg}} \frac{\partial K_{rg}}{\partial s_g} (\delta s_w + \delta s_o) \right] + q^G_{o,k,m} \left[1 + \frac{\mu_o B_o}{R_{so}\rho_{GS}} \frac{\partial}{\partial p} \left(\frac{R_{so}\rho_{GS}}{\mu_o B_o} \right) \delta p + \frac{1}{K_{ro}} \left(\frac{\partial K_{ro}}{\partial s_w} - \frac{\partial K_{ro}}{\partial s_g} \right) \delta s_w - \frac{1}{K_{ro}} \frac{\partial K_{ro}}{\partial s_g} \delta s_o \right] \right\}_l^{(n+1)} \delta_{k,m} \, d\mathbf{x} = Q_{G,k}.$$

The oil and liquid production rate controls are, respectively, linearized by

$$\sum_{m=1}^{M_{w,k}} \int_{V_{k,m}} \left\{ \mathrm{WI}_{k,m} \frac{K_{ro}\rho_{OS}}{\mu_o B_o} (\delta p_{bh,k} - \delta p) + q^G_{o,k,m} \left[1 + \frac{\mu_o B_o}{\rho_{OS}} \frac{\partial}{\partial p} \left(\frac{\rho_{OS}}{\mu_o B_o} \right) \delta p + \frac{1}{K_{ro}} \left(\frac{\partial K_{ro}}{\partial s_w} - \frac{\partial K_{ro}}{\partial s_g} \right) \delta s_w - \frac{1}{K_{ro}} \frac{\partial K_{ro}}{\partial s_g} \delta s_o \right] \right\}_l^{(n+1)} \delta_{k,m} \, d\mathbf{x} = Q_{O,k},$$

and

$$\sum_{m=1}^{M_{w,k}} \int_{V_{k,m}} \left\{ \mathrm{WI}_{k,m} \left[\frac{K_{rw}\rho_{WS}}{\mu_w B_w} + \frac{K_{ro}\rho_{OS}}{\mu_o B_o} \right] (\delta p_{bh,k} - \delta p) + q_{wk,m} \left[1 + \frac{\mu_w B_w}{\rho_{WS}} \frac{\partial}{\partial p} \left(\frac{\rho_{WS}}{\mu_w B_w} \right) \delta p + \frac{1}{K_{rw}} \frac{\partial K_{rw}}{\partial s_w} \delta s_w \right] + q_{ok,m} \left[1 + \frac{\mu_o B_o}{\rho_{WS}} \frac{\partial}{\partial p} \left(\frac{\rho_{OS}}{\mu_o B_o} \right) \delta p + \frac{1}{K_{ro}} \left(\frac{\partial K_{ro}}{\partial s_w} - \frac{\partial K_{ro}}{\partial s_g} \right) \delta s_w - \frac{1}{K_{ro}} \frac{\partial K_{ro}}{\partial s_g} \delta s_o \right] \right\}_l^{(n+1)} \delta_{k,m} \, d\mathbf{x} = Q_{L,k}.$$

Appendix B. Discretization of the governing equations

As noted, the discretization methods we use for the governing equations of the black oil model are the CVFA methods. We very briefly review the discretization of these equations by this method. For more details, refer to [6].

B.1. Undersaturated state

Let the lth iteration values of the water and oil potentials on boundary e_{ij} of a control volume V_i at the $(n+1)$th time step be approximated by (3.17) and the lth iteration values of the increments δp, δs_w, and δp_b be approximated by (3.18). Then the linearized governing equations under the undersaturated state given in Appendix A.1 can be discretized as follows:

$$\begin{aligned}
&\sum_{j=1}^{N_i} \sum_{r=0}^{R_{ij}} \int_{e_{ij}} \left\{ \frac{KK_{rw}}{\mu_w} \frac{\rho_{WS}}{B_w} + KK_{rw} \frac{\partial}{\partial p} \left(\frac{\rho_{WS}}{\mu_w B_w} \right) \delta p + \frac{K\rho_{WS}}{\mu_w B_w} \frac{\partial K_{rw}}{\partial s_w} \delta s_w \right\}_l^{(n+1)} (\Phi^i_{wj,r})_l^{(n+1)} \nabla \phi^i_{j,r}(\mathbf{x}) \cdot \mathbf{n} \, dA \\
&+ \sum_{j=1}^{N_i} \sum_{r=0}^{R_{ij}} \int_{e_{ij}} \left[\frac{KK_{rw}}{\mu_w} \frac{\rho_{WS}}{B_w} (\delta p^i_{j,r}) \right]_l^{(n+1)} \nabla \phi^i_{j,r}(\mathbf{x}) \cdot \mathbf{n} \, dA - \sum_{j=1}^{N_i} \sum_{r=0}^{R_{ij}} \int_{e_{ij}} \left[\frac{KK_{rw}}{\mu_w} \frac{\rho_{WS}}{B_w} \left(\frac{\partial p_{cow}}{\partial s_w} \delta s_w \right)^i_{j,r} \right]_l^{(n+1)} \\
&\times \nabla \phi^i_{j,r}(\mathbf{x}) \cdot \mathbf{n} \, dA + \sum_{k=1}^{N_w} \sum_{m=1}^{M_{w,k}} \int_{V_i} \left\{ q_{w,k,m} + \frac{\mu_w B_w}{\rho_{WS}} q_{w,k,m} \times \frac{\partial}{\partial p} \left(\frac{\rho_{WS}}{\mu_w B_w} \right) \delta p. + \frac{q_{w,k,m}}{K_{rw}} \frac{\partial K_{rw}}{\partial s_w} \delta s_w \right. \\
&\left. + \mathrm{WI}_{k,m} \frac{K_{rw}\rho_{WS}}{\mu_w B_w} (\delta p_{bh,k} - \delta p) \right\}_l^{(n+1)} \delta_{k,m} \, d\mathbf{x} \\
&= \frac{V_i}{\Delta t_n} \left\{ \left(\phi \frac{\rho_{WS}}{B_w} s_w \right)_l^{(n+1)} - \left(\phi \frac{\rho_{WS}}{B_w} s_w \right)^{(n)} + \left(\phi \frac{\rho_{WS}}{B_w} \right)_l^{(n+1)} (\delta s_w)_l^{(n+1)} + \left[c_r \phi_a \frac{\rho_{WS}}{B_w} s_w + \phi s_w \frac{\partial}{\partial p} \left(\frac{\rho_{WS}}{B_w} \right) \right]_l^{(n+1)} (\delta p)_l^{(n+1)} \right\}_{\mathbf{x}=\mathbf{x}_i},
\end{aligned}$$

$$\begin{aligned}
&\sum_{j=1}^{N_i} \sum_{r=0}^{R_{ij}} \int_{e_{ij}} \left\{ \frac{KK_{ro}}{\mu_o} \frac{\rho_{OS}}{B_o} + KK_{ro} \frac{\partial}{\partial p} \left(\frac{\rho_{OS}}{\mu_o B_o} \right) \delta p + \frac{K\rho_{OS}}{\mu_o B_o} \frac{\partial K_{ro}}{\partial s_w} \delta s_w + KK_{ro} \frac{\partial}{\partial p_b} \left(\frac{\rho_{OS}}{\mu_o B_o} \right) \delta p_b \right\}_l^{(n+1)} \\
&\times (\Phi^i_{oj,r})_l^{(n+1)} \nabla \phi^i_{j,r}(\mathbf{x}) \cdot \mathbf{n} \, dA + \sum_{j=1}^{N_i} \sum_{r=0}^{R_{ij}} \int_{e_{ij}} \left[\frac{KK_{ro}}{\mu_o} \frac{\rho_{OS}}{B_o} (\delta p^i_{j,r}) \right]_l^{(n+1)} \nabla \phi^i_{j,r}(\mathbf{x}) \cdot \mathbf{n} \, dA \\
&+ \sum_{k=1}^{N_w} \sum_{m=1}^{M_{w,k}} \int_{V_i} \left\{ q_{o,k,m} - \mathrm{WI}_{k,m} \frac{K_{ro}\rho_{OS}}{\mu_o B_o} (\delta p - \delta p_{bh,k}) + \frac{\mu_o B_o}{\rho_{OS}} q_{o,k,m} \frac{\partial}{\partial p} \left(\frac{\rho_{OS}}{\mu_o B_o} \right) \delta p + \frac{q_{o,k,m}}{K_{ro}} \frac{\partial K_{ro}}{\partial s_w} \delta s_w \right. \\
&\left. + \frac{\mu_o B_o}{\rho_{OS}} q_{o,k,m} \frac{\partial}{\partial p_b} \left(\frac{\rho_{OS}}{\mu_o B_o} \right) \delta p_b \right\}_l^{(n+1)} \delta_{k,m} \, d\mathbf{x} \\
&= \frac{V_i}{\Delta t_n} \left\{ \left(\phi \frac{\rho_{OS}}{B_o} s_o \right)_l^{(n+1)} - \left(\phi \frac{\rho_{OS}}{B_o} s_o \right)^{(n)} + \left[\phi s_o \frac{\partial}{\partial p_b} \left(\frac{\rho_{OS}}{B_o} \right) \right]_l^{(n+1)} (\delta p_b)_l^{(n+1)} + \left[c_r \phi_a \frac{\rho_{OS}}{B_o} s_o + \phi s_o \frac{\partial}{\partial p} \left(\frac{\rho_{OS}}{B_o} \right) \right]_l^{(n+1)} (\delta p)_l^{(n+1)} \right. \\
&\left. - \left(\phi \frac{\rho_{OS}}{B_o} \right)_l^{(n+1)} (\delta s_w)_l^{(n+1)} \right\}_{\mathbf{x}=\mathbf{x}_i},
\end{aligned}$$

and

$$\sum_{j=1}^{N_i}\sum_{r=0}^{R_{ij}}\int_{e_{ij}}\left\{\frac{KK_{ro}}{\mu_o}\frac{R_{so}\rho_{GS}}{B_o}+KK_{ro}\frac{\partial}{\partial p}\left(\frac{R_{so}\rho_{GS}}{\mu_oB_o}\right)\delta p\right.$$
$$\left.+\frac{KR_{so}\rho_{GS}}{\mu_oB_o}\frac{\partial K_{ro}}{\partial s_w}\delta s_w+KK_{ro}\frac{\partial}{\partial p_b}\left(\frac{R_{so}\rho_{GS}}{\mu_oB_o}\right)\delta p_b\right\}_l^{(n+1)}$$
$$\times(\Phi^i_{oj,r})_l^{(n+1)}\nabla\phi^i_{j,r}(\mathbf{x})\cdot\mathbf{n}\,dA$$
$$+\sum_{j=1}^{N_i}\sum_{r=0}^{R_{ij}}\int_{e_{ij}}\left[\frac{KK_{ro}}{\mu_o}\frac{R_{so}\rho_{GS}}{B_o}(\delta p^i_{j,r})\right]_l^{(n+1)}\nabla\phi^i_{j,r}(\mathbf{x})\cdot\mathbf{n}\,dA$$
$$+\sum_{k=1}^{N_w}\sum_{m=1}^{M_{w,k}}\int_{V_i}\left\{q^G_{o,k,m}+\frac{\mu_oB_o}{R_{so}\rho_{GS}}q^G_{o,k,m}\frac{\partial}{\partial p}\left(\frac{R_{so}\rho_{GS}}{\mu_oB_o}\right)\delta p\right.$$
$$+\frac{q^G_{o,k,m}}{K_{ro}}\frac{\partial K_{ro}}{\partial s_w}\delta s_w+\frac{\mu_oB_o}{R_{so}\rho_{GS}}q^G_{o,k,m}\frac{\partial}{\partial p_b}\left(\frac{R_{so}\rho_{GS}}{\mu_oB_o}\right)\delta p_b$$
$$\left.+\mathrm{WI}_{k,m}\frac{K_{ro}R_{so}\rho_{GS}}{\mu_oB_o}(\delta p_{bh,k}-\delta p)\right\}\delta_{k,m}\,d\mathbf{x}$$
$$=\frac{V_i}{\Delta t_n}\left\{\left(\phi\frac{R_{so}\rho_{GS}}{B_o}s_o\right)_l^{(n+1)}-\left(\phi\frac{R_{so}\rho_{GS}}{B_o}s_o\right)^{(n)}\right.$$
$$+\left[c_r\phi_a\frac{R_{so}\rho_{GS}}{B_o}s_o+\phi s_o\frac{\partial}{\partial p}\left(\frac{R_{so}\rho_{GS}}{B_o}\right)\right]_l^{(n+1)}(\delta p)_l^{(n+1)}$$
$$-\left(\phi\frac{R_{so}\rho_{GS}}{B_o}s_o\right)_l^{(n+1)}(\delta s_w)_l^{(n+1)}$$
$$\left.+\left[\phi s_o\frac{\partial}{\partial p_b}\left(\frac{R_{so}\rho_{GS}}{B_o}\right)\right]_l^{(n+1)}(\delta p_b)_l^{(n+1)}\right\}_{\mathbf{x}=\mathbf{x}_i}.$$

B.2. Saturated state

Similarly, we use (3.20) and (3.21) to have

$$\sum_{j=1}^{N_i}\sum_{r=0}^{R_{ij}}\int_{e_{ij}}\left\{\frac{KK_{rw}}{\mu_w}\frac{\rho_{WS}}{B_w}+KK_{rw}\frac{\partial}{\partial p}\left(\frac{\rho_{WS}}{\mu_wB_w}\right)\delta p\right.$$
$$\left.+\frac{K\rho_{WS}}{\mu_wB_w}\frac{\partial K_{rw}}{\partial s_w}\delta s_w\right\}_l^{(n+1)}\times(\Phi^i_{wj,r})_l^{(n+1)}\nabla\phi^i_{j,r}(\mathbf{x})\cdot\mathbf{n}\,dA$$
$$+\sum_{j=1}^{N_i}\sum_{r=0}^{R_{ij}}\int_{e_{ij}}\left[\frac{KK_{rw}}{\mu_w}\frac{\rho_{WS}}{B_w}(\delta p^i_{j,r})\right]_l^{(n+1)}\nabla\phi^i_{j,r}(\mathbf{x})\cdot\mathbf{n}\,dA$$
$$-\sum_{j=1}^{N_i}\sum_{r=0}^{R_{ij}}\int_{e_{ij}}\left[\frac{KK_{rw}}{\mu_w}\frac{\rho_{WS}}{B_w}\left(\frac{\partial p_{cow}}{\partial s_w}\delta s_w\right)^i_{j,r}\right]_l^{(n+1)}\nabla\phi^i_{j,r}(\mathbf{x})\cdot\mathbf{n}\,dA$$
$$+\sum_{k=1}^{N_w}\sum_{m=1}^{M_{w,k}}\int_{V_i}\left\{q_{w,k,m}+\frac{\mu_wB_w}{\rho_{WS}}q_{w,k,m}\frac{\partial}{\partial p}\left(\frac{\rho_{WS}}{\mu_wB_w}\right)\delta p\right.$$
$$\left.+\frac{q_{w,k,m}}{K_{rw}}\frac{\partial K_{rw}}{\partial s_w}\delta s_w+\mathrm{WI}_{k,m}\frac{K_{rw}\rho_{WS}}{\mu_wB_w}(\delta p_{bh,k}-\delta p)\right\}_l^{(n+1)}\delta_{k,m}\,d\mathbf{x}$$
$$=\frac{V_i}{\Delta t_n}\left\{\left(\phi\frac{\rho_{WS}}{B_w}s_w\right)_l^{(n+1)}-\left(\phi\frac{\rho_{WS}}{B_w}s_w\right)^{(n)}\right.$$
$$+\left(\phi\frac{\rho_{WS}}{B_w}\right)_l^{(n+1)}(\delta s_w)_l^{(n+1)}$$
$$\left.+\left[c_r\phi_a\frac{\rho_{WS}}{B_w}s_w+\phi s_w\frac{\partial}{\partial p}\left(\frac{\rho_{WS}}{B_w}\right)\right]_l^{(n+1)}(\delta p)_l^{(n+1)}\right\}_{\mathbf{x}=\mathbf{x}_i},$$

$$\sum_{j=1}^{N_i}\sum_{r=0}^{R_{ij}}\int_{e_{ij}}\left\{\frac{KK_{ro}}{\mu_o}\frac{\rho_{OS}}{B_o}+KK_{ro}\frac{\partial}{\partial p}\left(\frac{\rho_{OS}}{\mu_oB_o}\right)\delta p\right.$$
$$-\frac{K\rho_{OS}}{\mu_oB_o}\frac{\partial K_{ro}}{\partial s_g}\delta s_o+\frac{K\rho_{OS}}{\mu_oB_o}\left(\frac{\partial K_{ro}}{\partial s_w}-\frac{\partial K_{ro}}{\partial s_g}\right)\delta s_w\Big\}_l^{(n+1)}$$
$$\times(\Phi^i_{oj,r})_l^{(n+1)}\nabla\phi^i_{j,r}(\mathbf{x})\cdot\mathbf{n}\,dA$$
$$+\sum_{j=1}^{N_i}\sum_{r=0}^{R_{ij}}\int_{e_{ij}}\left[\frac{KK_{ro}}{\mu_o}\frac{\rho_{OS}}{B_o}(\delta p^i_{j,r})\right]_l^{(n+1)}\nabla\phi^i_{j,r}(\mathbf{x})\cdot\mathbf{n}\,dA$$
$$+\sum_{k=1}^{N_w}\sum_{m=1}^{M_{w,k}}\int_{V_i}\left\{q_{o,k,m}+\frac{\mu_oB_o}{\rho_{OS}}q_{o,k,m}\frac{\partial}{\partial p}\left(\frac{\rho_{OS}}{\mu_oB_o}\right)\delta p\right.$$
$$-\frac{q_{o,k,m}}{K_{ro}}\frac{\partial K_{ro}}{\partial s_g}\delta s_o+\frac{q_{o,k,m}}{K_{ro}}\left(\frac{\partial K_{ro}}{\partial s_w}-\frac{\partial K_{ro}}{\partial s_g}\right)\delta s_w$$
$$\left.+\mathrm{WI}_{k,m}\frac{K_{ro}\rho_{OS}}{\mu_oB_o}(\delta p_{bh,k}-\delta p)\right\}_l^{(n+1)}\delta_{k,m}\,d\mathbf{x}$$
$$=\frac{V_i}{\Delta t_n}\left\{\left(\phi\frac{\rho_{OS}}{B_o}s_o\right)_l^{(n+1)}-\left(\phi\frac{\rho_{OS}}{B_o}s_o\right)^{(n)}\right.$$
$$+\left(\phi\frac{\rho_{OS}}{B_o}\right)_l^{(n+1)}(\delta s_o)_l^{(n+1)}+\left[c_r\phi_a\frac{\rho_{OS}}{B_o}s_o\right.$$
$$\left.\left.+\phi s_o\frac{\partial}{\partial p}\left(\frac{\rho_{OS}}{B_o}\right)\right]_l^{(n+1)}(\delta p)_l^{(n+1)}\right\}_{\mathbf{x}=\mathbf{x}_i},$$

and

$$\sum_{j=1}^{N_i}\sum_{r=0}^{R_{ij}}\int_{e_{\bar{z}ij}}\left\{\frac{KK_{rg}}{\mu_g}\frac{\rho_{GS}}{B_g}+KK_{rg}\frac{\partial}{\partial p}\left(\frac{\rho_{GS}}{\mu_gB_g}\right)\delta p\right.$$
$$\left.-\frac{K\rho_{GS}}{\mu_gB_g}\frac{\partial K_{rg}}{\partial s_g}\delta s_w-\frac{K\rho_{GS}}{\mu_gB_g}\frac{\partial K_{rg}}{\partial s_g}\delta s_o\right\}_l^{(n+1)}$$
$$\times(\Phi^i_{gj,r})_l^{(n+1)}\nabla\phi^i_{j,r}(\mathbf{x})\cdot\mathbf{n}\,dA$$
$$+\sum_{j=1}^{N_i}\sum_{r=0}^{R_{ij}}\int_{e_{ij}}\left[\frac{KK_{rg}}{\mu_g}\frac{\rho_{GS}}{B_g}(\delta p^i_{j,r})\right]_l^{(n+1)}\nabla\phi^i_{j,r}(\mathbf{x})\cdot\mathbf{n}\,dA$$
$$-\sum_{j=1}^{N_i}\sum_{r=0}^{R_{ij}}\int_{e_{ij}}\left[\frac{KK_{rg}}{\mu_g}\frac{\rho_{GS}}{B_g}\left(\frac{\partial p_{cgo}}{\partial s_g}\delta s_w+\frac{\partial p_{cgo}}{\partial s_g}\delta s_o\right)^i_{j,r}\right]_l^{(n+1)}$$
$$\times\nabla\phi^i_{j,r}(\mathbf{x})\cdot\mathbf{n}\,dA+\sum_{j=1}^{N_i}\sum_{r=0}^{R_{ij}}\int_{e_{ij}}\left\{\frac{KK_{ro}}{\mu_o}\frac{R_{so}\rho_{GS}}{B_o}\right.$$
$$+KK_{ro}\frac{\partial}{\partial p}\left(R_{so}\frac{\rho_{GS}}{\mu_oB_o}\right)\delta p-\frac{KR_{so}\rho_{GS}}{\mu_oB_o}\frac{\partial K_{ro}}{\partial s_g}\delta s_o$$
$$\left.+\frac{KR_{so}\rho_{GS}}{\mu_oB_o}\left(\frac{\partial K_{ro}}{\partial s_w}-\frac{\partial K_{ro}}{\partial s_g}\right)\delta s_w\right\}_l^{(n+1)}(\Phi^i_{oj,r})_l^{(n+1)}$$
$$\times\nabla\phi^i_{j,r}(\mathbf{x})\cdot\mathbf{n}\,dA+\int_{\partial V_i}\left[\frac{KK_{ro}}{\mu_o}\frac{R_{so}\rho_{GS}}{B_o}(\delta p^i_{j,r})\right]_l^{(n+1)}$$
$$\times\nabla\phi^i_{j,r}(\mathbf{x})\cdot\mathbf{n}\,dA$$

$$
\begin{aligned}
&+\sum_{k=1}^{N_w}\sum_{m=1}^{M_{w,k}}\int_{V_i}\left\{q^G_{g,k,m}+\mathrm{WI}_{k,m}\frac{K_{rg}\rho_{GS}}{\mu_g B_g}(\delta p_{bh,k}-\delta p)\right.\\
&+\frac{\mu_g B_g}{\rho_{GS}}q^G_{g,k,m}\frac{\partial}{\partial p}\left(\frac{\rho_{GS}}{\mu_g B_g}\right)\delta p\\
&\left.-\frac{q^G_{g,k,m}}{K_{rg}}\frac{\partial K_{rg}}{\partial s_g}(\delta s_w+\delta s_o)\right\}^{(n+1)}_{l}\delta_{k,m}\,\mathrm{d}\mathbf{x}\\
&+\sum_{k=1}^{N_w}\sum_{m=1}^{M_{w,k}}\int_{V_i}\left\{q^G_{o,k,m}+\mathrm{WI}_{k,m}\frac{K_{ro}R_{so}\rho_{GS}}{\mu_o B_o}(\delta p_{bh,k}-\delta p)\right.\\
&-\frac{q^G_{o,k,m}}{K_{ro}}\frac{\partial K_{ro}}{\partial s_g}\delta s_o+\frac{\mu_o B_o}{R_{so}\rho_{GS}}q^G_{o,k,m}\frac{\partial}{\partial p}\left(\frac{R_{so}\rho_{GS}}{\mu_o B_o}\right)\delta p\\
&\left.+\frac{q^G_{o,k,m}}{K_{ro}}\left(\frac{\partial K_{ro}}{\partial s_w}-\frac{\partial K_{ro}}{\partial s_g}\right)\delta s_w\right\}^{(n+1)}_{l}\delta_{k,m}\,\mathrm{d}\mathbf{x}\\
&=\frac{V_i}{\Delta t_n}\left\{\left(\phi\frac{\rho_{GS}}{B_g}s_g\right)^{(n+1)}_{l}-\left(\phi\frac{\rho_{GS}}{B_g}s_g\right)^{(n)}-\left(\phi\frac{\rho_{GS}}{B_g}\right)^{(n+1)}_{l}\right.\\
&\times(\delta s_w)^{(n+1)}_{l}+\left[c_r\phi_a\frac{\rho_{GS}}{B_g}s_g+\phi s_g\frac{\partial}{\partial p}\left(\frac{\rho_{GS}}{B_g}\right)\right]^{(n+1)}_{l}\\
&\left.\times(\delta p)^{(n+1)}_{l}-\left(\phi\frac{\rho_{GS}}{B_g}\right)^{(n+1)}_{l}(\delta s_o)^{(n+1)}_{l}\right\}_{\mathbf{x}=\mathbf{x}_i}\\
&+\frac{V_i}{\Delta t_n}\left\{\left(\phi\frac{R_{so}\rho_{GS}}{B_o}s_o\right)^{(n+1)}_{l}-\left(\phi\frac{R_{so}\rho_{GS}}{B_o}s_o\right)^{(n)}\right.\\
&+\left[c_r\phi_a\frac{R_{so}\rho_{GS}}{B_o}s_o+\phi s_o\frac{\partial}{\partial p}\left(\frac{R_{so}\rho_{GS}}{B_o}\right)\right]^{(n+1)}_{l}(\delta p)^{(n+1)}_{l}\\
&\left.+\left(\phi\frac{R_{so}\rho_{GS}}{B_o}\right)^{(n+1)}_{l}(\delta s_o)^{(n+1)}_{l}\right\}_{\mathbf{x}=\mathbf{x}_i}.
\end{aligned}
$$

References

[1] Aziz K, Settari A. Petroleum reservoir simulation. London: Applied Science, Publishers Ltd; 1979.

[2] Fanchi JR. Principles of applied reservoir simulation. 2nd ed. Gulf Professional Publishing; 2001.

[3] Fung LS, Hiebert AD, Nghiem L. Reservoir simulation with a control volume finite element method, SPE 21224, the 11th SPE Symposium on Reservoir Simulation, Anaheim, 17–20 February 1991.

[4] Heinrich B. Finite difference methods on irregular networks. Basel: Birkhauser; 1987.

[5] Li B. A control volume function approximation method for reservoir simulation with flexible grids, Dissertation, Department of Mathematics, Southern Methodist University, Dallas, Texas, 2003.

[6] Li B, Chen Z, Huan G. Control volume function approximation methods and their applications to modeling porous media flow I: The two-phase flow. Adv Water Resour 2003;26:435–44.

[7] Li B, Chen Z, Huan G. The sequential method for the black oil model on unstructured grids. J Comput Phys 2003;192:36–72.

[8] Odeh AS. Comparison of solutions to a three-dimensional black-oil reservoir problem. J Petroleum Technol 1981:13–25.

[9] Peaceman DW. Fundamentals of numerical reservoir simulation. New York: Elsevier; 1977.

[10] Peaceman DW. Interpretation of well-block pressures in numerical reservoir simulation, SPE 6893, 52nd Annual Fall Technical Conference and Exhibition, Denver, 1977.

[11] Vinsome PW. ORTHOMIN: An iterative method for solving sparse sets of simultaneous linear equations, Paper SPE 5729, Presented at the SPE Symposium on Reservoir Simulation held in Los Angles, California, 19–20 February 1976.

[12] Weinstein HG, Chappelear JE, Nolen JS. Second comparative solution project: A three-phase coning study. J Petroleum Technol 1986:345–53.